

The Evolution of the 10–11 June 1985 PRE-STORM Squall Line: Initiation, Development of Rear Inflow, and Dissipation

SCOTT A. BRAUN AND ROBERT A. HOUZE JR.

Department of Atmospheric Sciences, University of Washington, Seattle, Washington

(Manuscript received 12 December 1995, in final form 12 August 1996)

ABSTRACT

Mesoscale analysis of surface observations and mesoscale modeling results show that the 10–11 June squall line, contrary to prior studies, did not form entirely ahead of a cold front. The primary environmental features leading to the initiation and organization of the squall line were a low-level trough in the lee of the Rocky Mountains and a midlevel short-wave trough. Three additional mechanisms were active: a southeastward-moving cold front formed the northern part of the line, convection along the edge of cold air from prior convection over Oklahoma and Kansas formed the central part of the line, and convection forced by convective outflow near the lee trough axis formed the southern portion of the line.

Mesoscale model results show that the large-scale environment significantly influenced the mesoscale circulations associated with the squall line. The qualitative distribution of along-line velocities within the squall line is attributed to the larger-scale circulations associated with the lee trough and midlevel baroclinic wave. Ambient rear-to-front (RTF) flow to the rear of the squall line, produced by the squall line's nearly perpendicular orientation to strong westerly flow at upper levels, contributed to the exceptional strength of the rear inflow in this storm. The mesoscale model results suggest that the effects of the line ends and the generation of horizontal buoyancy gradients at the back edge of the system combined with this ambient RTF flow to concentrate the strongest convection and back-edge sublimative cooling along the central portion of the line, which then produced a core of maximum rear inflow with a horizontal scale of approximately 100–200 km. The formation of the rear-inflow core followed the onset of strong sublimative cooling at the back edge of the storm and suggests that the rear inflow maximum was significantly influenced by microphysical processes. In a sensitivity test, in which sublimative cooling was turned off midway through the simulation, the core of strong rear inflow failed to form and the squall line rapidly weakened.

The evolution of the low-level mesoscale to synoptic-scale pressure field contributed to the dissipation of the squall line. Cyclogenesis occurred over Missouri, ahead of the squall line, and caused the presquall flow to veer from southeasterly to southwesterly, which decreased the low-level inflow and line-normal vertical wind shear. The reduction in low-level wind shear decreased the effectiveness of the cold pool in sustaining deep convection along the gust front.

1. Introduction

A common feature of mesoscale convective systems (MCSs) with leading-line/trailing stratiform precipitation structure is a midlevel jet of rear-to-front (RTF) storm-relative airflow that extends from within the stratiform precipitation region into the convective region. Occasionally, the RTF flow is confined entirely within the precipitation regions (Chong et al. 1987), that is, it is an internal feature of the MCS and is hypothesized to result from processes internal to the storm (LeMone 1983; LeMone et al. 1984; Smull and Houze 1987). On other occasions, RTF flow is observed across the back edge of the stratiform precipitation region and was termed *rear inflow* by Smull and Houze (1987). In this study, we use the term rear inflow exclusively to de-

scribe that component of the RTF flow near the back edge of the stratiform precipitation region. The strength of this rear inflow varies substantially from case to case (Smull and Houze 1987). Rear inflow sometimes combines with the internally generated RTF flow to form a continuous RTF flow across the stratiform precipitation region. Rear inflow is occasionally observed to exceed the strength of the internal RTF flow such that maximum RTF velocities occur at the back edge of the stratiform precipitation region (e.g., Smull and Houze 1985; Rutledge et al. 1988; Smull and Augustine 1993).

The development of the internal RTF flow is associated with the formation of a mostly hydrostatically induced midlevel mesolow located to the rear of the convective line beneath the sloping convective updrafts; alternatively, it can be viewed in terms of the generation of horizontal vorticity by buoyancy gradients along the back edge of the system (LeMone 1983; LeMone et al. 1984; Roux 1985; Fovell and Ogura 1988; Lafore and Moncrieff 1989; Weisman 1992; Braun and Houze

Corresponding author address: Dr. Scott A. Braun, National Center for Atmospheric Research, P.O. Box 3000, Boulder, CO 80307-3000.

1994; Yang and Houze 1995). Several cloud-resolving modeling studies have shown that aspects of the rear inflow are sensitive to ice microphysical processes (Chen and Cotton 1988; Lafore and Moncrieff 1989; Szeto and Cho 1994; Yang and Houze 1995). Mesoscale modeling studies by Zhang et al. (1989, hereafter ZGP) and Zhang and Gao (1989, hereafter ZG) suggest that microphysical processes were important in their simulation of a squall line, but that the structure of the rear inflow may also have been dependent on the presence of a midlevel mesoscale vortex within the stratiform precipitation region.

Several studies have considered the along-line variability of RTF jets in squall lines. Weisman (1993) demonstrated that along-line variability of RTF flow can occur in association with small-scale book-end vortices located at the ends of bow echoes with the strongest RTF flow located between the vortices. Skamarock et al. (1994) showed that a similar pattern of RTF flow occurs on somewhat larger scales with mesoscale vortices produced at the ends of convective lines. Midlevel cyclonic vortices are thought to be particularly important for cases possessing asymmetric leading-line/trailing stratiform precipitation structure, in which the strongest convection occurs along the southern portion of the line and the stratiform precipitation is concentrated behind the northern portion of the line (Houze et al. 1989; Brandes 1990; Houze et al. 1990; Skamarock et al. 1994; Loehrer and Johnson 1995). Klimowski (1994) found that midlevel RTF flow was maximum near high radar reflectivity cores in the convective line, which suggests that along-line variability may be partly related to the along-line variability of the intensity of convection. Circulations associated with the large-scale baroclinic environment may also be important in some cases (ZG).

While these previous studies have addressed aspects of the mechanisms for along-line variability, some questions remain about how the variability of the rear inflow is related to storm organization and to microphysical processes. Also, are environmental influences important for along-line variability of rear inflow?

This study uses results from a mesoscale model simulation (described in section 2) of the 10–11 June 1985 PRE-STORM¹ squall line, which exhibited exceptionally strong rear inflow (Smull and Houze 1987), to investigate the three-dimensional structure and evolution of the rear inflow. In this squall line, the RTF flow extended from midlevels (~650–350 mb, 3.5–8 km) at the back edge of the stratiform precipitation region, where its intensity was maximum, across the stratiform region near the 0°C level (4 km) and dipped downward to the surface in the convective region (Smull and Houze

1987; Rutledge et al. 1988; Biggerstaff and Houze 1993). That portion of the RTF flow observed within the leading portion of the stratiform region and in the convective region, the internal component of the RTF flow, owed its existence primarily to convective-scale thermodynamic and dynamic processes, diabatic heating, and the generation of a mesoscale low-pressure region beneath the sloping convective updrafts (LeMone 1983; LeMone et al. 1984; Smull and Houze 1987; Fovell and Ogura 1988; Lafore and Moncrieff 1989; Weisman 1992; Braun and Houze 1994). This development is not well resolved with the grid spacing of the current model (20 km). Consequently, the internal component of the RTF flow will not be examined. Our analysis focuses instead on the mesoscale structure of the rear inflow along the back edge of the stratiform precipitation region of the squall line.

Microphysical processes played a role in the development of the rear inflow in the 10–11 June squall line (ZG; Gallus and Johnson 1995; Yang and Houze 1995). ZGP, however, suggested that the location of the maximum rear inflow near the central portion of the squall line was related to a midlevel mesoscale vortex in the northern portion of the squall line. ZGP and Zhang (1992) showed that this vortex was present in the initial environment in association with a midlevel short-wave trough and was subsequently enhanced by the convective system. The results presented in section 4 suggest that the mesoscale structure of the rear inflow and the location of the strongest rear inflow along the central portion of the storm were not the direct result of this midlevel mesoscale vortex. Instead, the mesoscale structure of the rear inflow resulted primarily from a dynamic response to horizontal buoyancy gradients generated in the rear portion of the squall line. Line-end effects concentrated the most intense convection and back-edge sublimative cooling along the central portion of the storm and these factors led to the development of the most intense rear inflow there. This interpretation is based on an examination of the horizontal variability of the rear inflow relative to the hydrometeor, pressure, and buoyancy fields at middle to upper levels. Sensitivity of the mesoscale along-line variability of the rear inflow in the model to resolvable-scale sublimative cooling occurred because the large-scale environmental flow provided a significant contribution to the strength of the rear inflow above the 0°C level. The primary contribution of this study is to describe more completely the mesoscale aspects of the along-line variability of the rear inflow and the synergistic interaction between the large-scale environment and microphysical processes, which led to the exceptionally strong rear inflow in this case.

Since the exceptional strength of the rear inflow in this squall line was partially a result of the large-scale environment in which it formed, it is appropriate to describe the initial environment in some detail (section 3). Previous studies have suggested that the 10–11 June

¹ The Oklahoma–Kansas Preliminary Regional Experiment for Stormscale Operational and Research Meteorology was conducted in May and June 1985 (Cunning 1986).

squall line formed ahead of and parallel to an advancing cold front (Johnson and Hamilton 1988; ZGP; ZG). However, this study shows that the predominant features of the large-scale environment were actually a mid- to upper-level baroclinic wave passing over the Rocky Mountains (also noted by Johnson and Hamilton 1988 and ZGP) and a lee trough east of the Rockies at low levels. Within this lee-trough environment, three mechanisms were active in forcing convection along different parts of the squall line: 1) the northern end of the line formed in association with an advancing baroclinic zone, 2) the central portion of the line formed along cold outflow from prior convection in central Kansas and Oklahoma, and 3) the southern portion of the line appeared to form near a warm tongue of air associated with the lee trough and possibly along cold outflow from convection over central Colorado. While the cold-air forcing of the convection in the northern end of the line may have been associated with a weak cold front, a major portion of the line did not initiate along such a boundary.

In addition to its effects on the across-line [RTF and front-to-rear (FTR)] circulations within the squall line, the large-scale environment significantly influenced the along-line motions within the squall line (section 4b). In particular, the meso- α -scale² response to the lee trough near the surface, as well as the flow associated with the mid- to upper-level baroclinic wave, led to the development of a deep layer of northeasterly flow to the rear of the gust front and southwesterly flow ahead of and at upper levels within the squall line.

ZGP and ZG have suggested that the 10–11 June squall line weakened as it moved into an environment with less convective instability. We suggest that an additional mechanism, originally proposed by Johnson and Hamilton (1988), may have been active. Toward the dissipating stage, cyclogenesis began ahead of the squall line over Missouri (Zhang and Harvey 1995). As cyclogenesis proceeded, the low-level inflow into the squall line and the vertical shear normal to the line weakened. The weaker vertical shear may have subsequently modified the circulation at the gust front (Rotunno et al. 1988; Xu 1992; Xu and Moncrieff 1994) such that deep convection could no longer be supported.

2. Description of model and simulation parameters

The model used in this study is the workstation version of The Pennsylvania State University–National Center for Atmospheric Research (PSU–NCAR) non-hydrostatic mesoscale model (MM5, Version 1; Dudhia 1993). Two grid meshes were used with 28 vertical σ levels. The model height coordinate, σ , is defined as

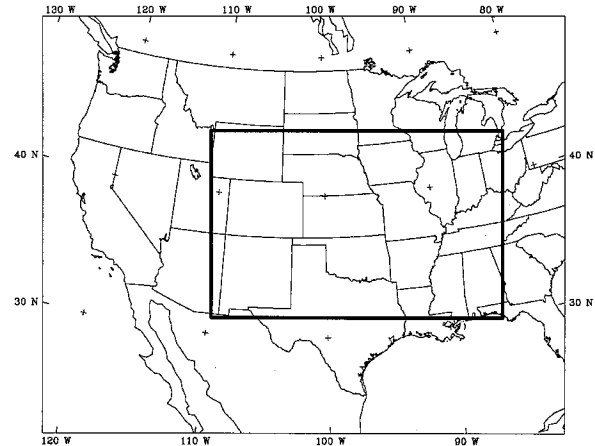


FIG. 1. Map of the coarse and fine mesh domains. The location of the fine (20-km horizontal resolution) mesh domain is indicated by the thick solid lines.

$= (p - p_{\text{top}})(p_{\text{sfc}} - p_{\text{top}})^{-1}$, where p is pressure, and p_{sfc} and p_{top} are the pressures at the surface and model top, respectively. For this simulation, p_{top} is 50 mb. The coarse grid, with a grid length of 60 km, had (x, y, σ) dimensions of $69 \times 55 \times 28$ and was centered at 38°N , 102°W . The fine grid, with a grid length of 20 km, had dimensions of $115 \times 73 \times 28$ and was located within the coarse mesh as shown in Fig. 1. A two-way interactive grid procedure was used (Zhang et al. 1986). The model topography was obtained from a Cressman-type objective analysis technique using 30' terrain resolution for the coarse mesh and 15' resolution for the fine mesh.

The model physics are essentially the same as those described in ZGP in their simulation of the 10–11 June squall line. The cumulus parameterization schemes used for the coarse and fine meshes are the Anthes–Kuo (Anthes et al. 1987) and Fritsch–Chappell (Fritsch and Chappell 1980) schemes, respectively. The grid-resolvable microphysical scheme (Zhang 1989) predicts mixing ratios of cloud water, cloud ice, rain, and snow but does not allow for mixed-phase precipitation processes. It is a bulk method (Houze 1993, 101–106), which assumes that the particles comprising a computed rain or snow mixing ratio have an exponential size distribution and that all particles in this distribution fall at the same terminal fall speed. This fall speed is estimated as the mass-weighted fall speed of the exponential distribution. The Blackadar “large-eddy exchange” planetary boundary layer parameterization was used (Zhang and Anthes 1982; Zhang and Fritsch 1986).

Our simulation differs from that of ZGP in the following ways. ZGP subjectively reduced the fall speeds for precipitation particles in the bulk microphysical scheme by 70%. No such reduction in fall speeds was used in our simulation. We calculate both longwave cooling and shortwave heating of the atmosphere every 30 min, neither was included in ZGP’s simulation. The horizontal resolution and number of vertical levels are

² The meso- α -scale, as defined by Orlanski (1975), ranges from 200 to 2000 km in horizontal extent.

20 km and 28 σ levels compared to 25 km and 19 σ levels in ZGP. The general behavior of the simulated squall line is similar to that described in ZGP and ZG. However, some differences do arise and are likely due to changes in the precipitation fall speeds. ZG found that without the 70% reduction of the precipitation fall speeds, their simulation produced a weaker surface mesohigh and wake low, a very intense presquall low, poorly developed rear inflow, and reduced squall-line propagation speed. Without the fall speed reduction, our simulation also produced a weaker surface mesohigh and wake low and the propagation speed was slower in the early stages of the storm. However, the simulation did not produce an intense presquall low but did produce a well-developed, weaker, descending rear-inflow jet. Weisman et al. (1997), who performed nonhydrostatic simulations of a squall line with grid resolutions ranging from 1 to 12 km, showed that varying the magnitude of the rain fall speed can have a substantial effect on coarse-grid simulations of squall lines. The effects of reducing the rain fall speeds were to increase the rain mixing ratios and the evaporation rates of rain water, which shortened the delay in the growth of the squall line in the coarse-grid simulations. However, Weisman et al. (1997) showed that the coarse-grid simulations (including the full fall velocity) tended to produce stronger mesoscale circulations than their finer grid counterparts. It is uncertain how the enhanced rain water evaporation caused by decreasing rain fall speeds by 70% in coarse-grid simulations might affect these mesoscale circulations. Furthermore, there is currently no physical basis for determining the appropriate magnitude of the fall speed reduction. Because of uncertainties in the benefits of reducing the fall speeds, as well as in the appropriate magnitude of the fall speed reduction, we have opted to use the full precipitation fall speed in this study.

A 24-h control simulation and two model sensitivity tests were initialized from National Center for Environmental Prediction (NCEP, formerly known as the National Meteorological Center) global analyses at 1200 UTC 10 June 1985. Boundary conditions at NCEP analysis times were similarly obtained every 12 h beginning at 1200 UTC 10 June and ending 1200 UTC 11 June. At all other times, boundary conditions were obtained by linear interpolation between analysis times. The NCEP fields at mandatory levels³ were horizontally interpolated to the coarse mesh and vertically interpolated to the following additional pressure levels: 975, 950, 925, 900, 800, 750, 600, 550, 450, and 350 mb. The interpolated NCEP analyses, which served as first-guess fields, were then improved by incorporating surface and upper-air observations into the analyses using a Cress-

man-type analysis scheme (Benjamin and Seaman 1985). Superadiabatic layers below 500 mb were removed by first comparing the potential temperature at 500 mb with that of the level immediately below. If the potential temperature at the lower level exceeded that at the upper level, it was adjusted to a value 0.1°C less than the value at the upper level. This process was repeated at successively lower levels until the surface was reached (Manning and Haagenson 1992). The fine mesh was initialized in the same manner except that the improved coarse mesh analyses were used as the first-guess fields. The analyses were interpolated to the model σ levels. To reduce noise early in the model integration, the vertically integrated mean divergence was removed from each column (Washington and Baumhefner 1975). Winds were obtained from the modified divergence fields.

Along with the control run described above, two additional simulations were performed to test the effects of resolvable-scale evaporative and sublimative cooling on the development of rear inflow [section 4c(3)]. In simulations designated NOSUB and NOEVP, the effects of grid-resolvable sublimation and evaporation, respectively, were removed from the thermodynamic equation but were retained in the microphysical equations. Both simulations were started from the 0000 UTC (12 h; in the discussion below, model times are provided where appropriate within parentheses following the verification time) model fields. At this time, the simulated squall line was in its developing stage, but significant rear inflow and grid-resolvable cooling had not yet begun. By beginning these simulations at this time, the effects of these microphysical processes on identically developed squall lines could be examined.

3. Lee trough formation and squall-line initiation

In this section, we describe the meso- α -scale conditions at the time of the initiation of the squall line. In particular, we trace the early development of a lee trough and describe its role in the initiation and development of the 10–11 June squall line. Johnson and Hamilton (1988) and ZGP have described the broader synoptic-scale setting for this case.

a. Mesoscale surface analyses and satellite observations

Figures 2 and 3a show the infrared satellite image and surface mesoscale analysis, respectively, for 1500 UTC 10 June, approximately 4 h before the initiation of the 10–11 June squall line. The infrared image shows an extensive cloud shield extending from southeastern Utah to Minnesota. This cloud shield was approximately oriented along a 700-mb trough axis. A large MCS was located over central and eastern Kansas and Oklahoma and is referred to as the 10 June MCS. The sea level pressure analysis shows a weak low located over eastern

³ The mandatory levels are the surface, 1000, 850, 700, 500, 400, 300, 250, 200, 150, 100, 70, and 50 mb.

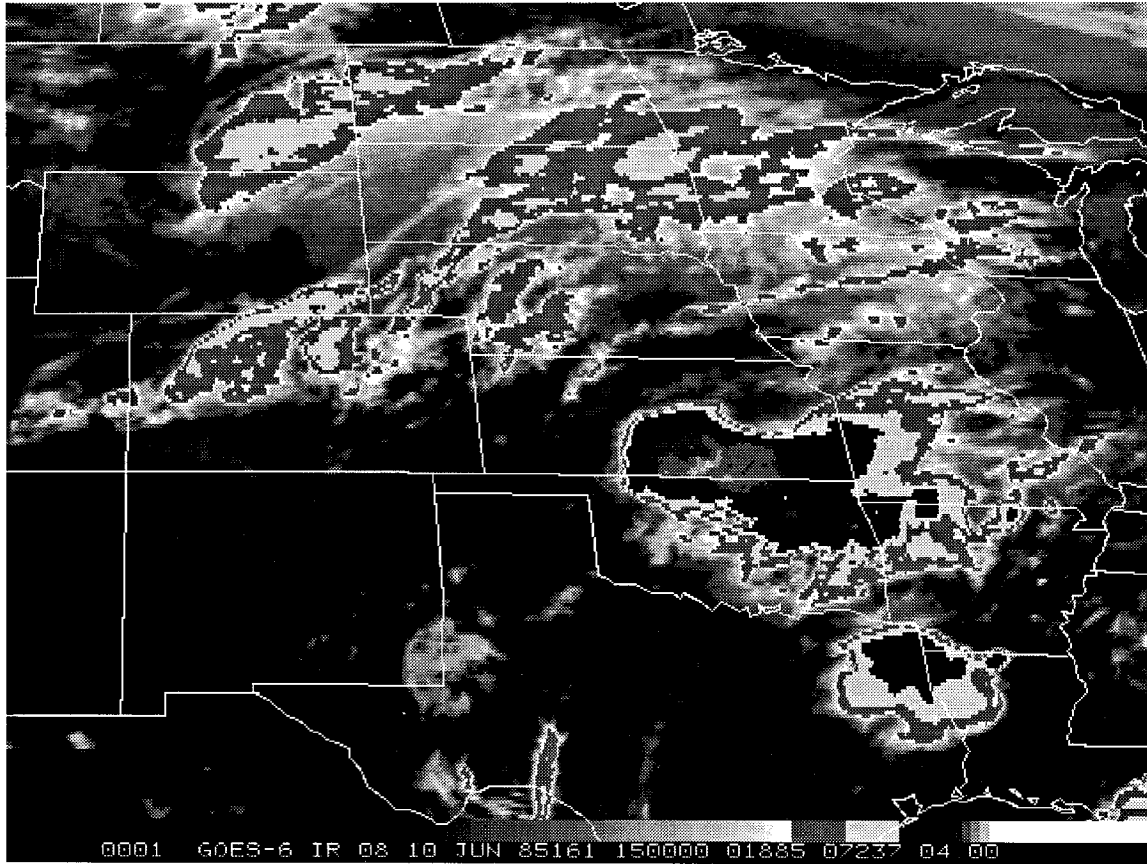


FIG. 2. Enhanced infrared satellite image for 1500 UTC 10 June 1985.

New Mexico and Colorado, with a trough extending northward into western Nebraska. A distinct wind shift occurred along this northern trough, with northwesterly flow to the west and southeasterly flow to the east of the trough axis. The potential temperature field shows a weak baroclinic zone over Wyoming and western Nebraska, with the front just crossing the northern border of Colorado. A weak but developing cold pool was located over Kansas and Oklahoma and was associated with the 10 June MCS.

At 1800 UTC [Fig. 3b; see Fig. 6b of ZGP for satellite image], the cloud band associated with the midlevel trough moved farther eastward and the cloud-top temperatures associated with the 10 June MCS increased. The sea level pressure field shows a deepening of the low over northeastern New Mexico. The trough continued to extend northward into Nebraska and to show a distinct wind shift across its axis. The strong cyclonic vorticity implied by this wind shift was manifested as a low-level mesoscale vortex in the simulation of ZGP. The baroclinic zone extended into northeastern Colorado and western Nebraska. The northwesterly to northerly flow west of the trough axis was advecting potentially cooler air into eastern Colorado; however, this northerly flow also extended southward into the poten-

tially warmer air near the low center. The western boundary of the cold air associated with the 10 June MCS was clearly defined by a strong gradient of potential temperature along its edge in western Kansas.

By 1900 UTC (Fig. 3c), pressures increased west of the trough axis in western Nebraska and northeastern Colorado. The potential temperature gradient in eastern Colorado intensified, in part because of convergence within the baroclinic zone. However, cloud cover reports indicate that differential solar heating also contributed to the increased gradients. The potential temperature gradient along the edge of the cold air over western Kansas and Oklahoma also intensified and was oriented nearly perpendicular to the leading edge of the cold air over northeastern Colorado. The frontogenesis along this cold-outflow boundary was also enhanced by differential radiative heating as the cloud cover over central Oklahoma and Kansas inhibited heating rates while solar heating was maximum in the warm trough, where there was little or no cloud cover (ZGP). These two cold-air boundaries intersected over northwestern Kansas. A second cold-outflow boundary, identified in the analysis of higher resolution surface mesonet data over Oklahoma and Kansas by Johnson and Hamilton (1988), formed in central Kansas. Johnson and Hamilton (1988)

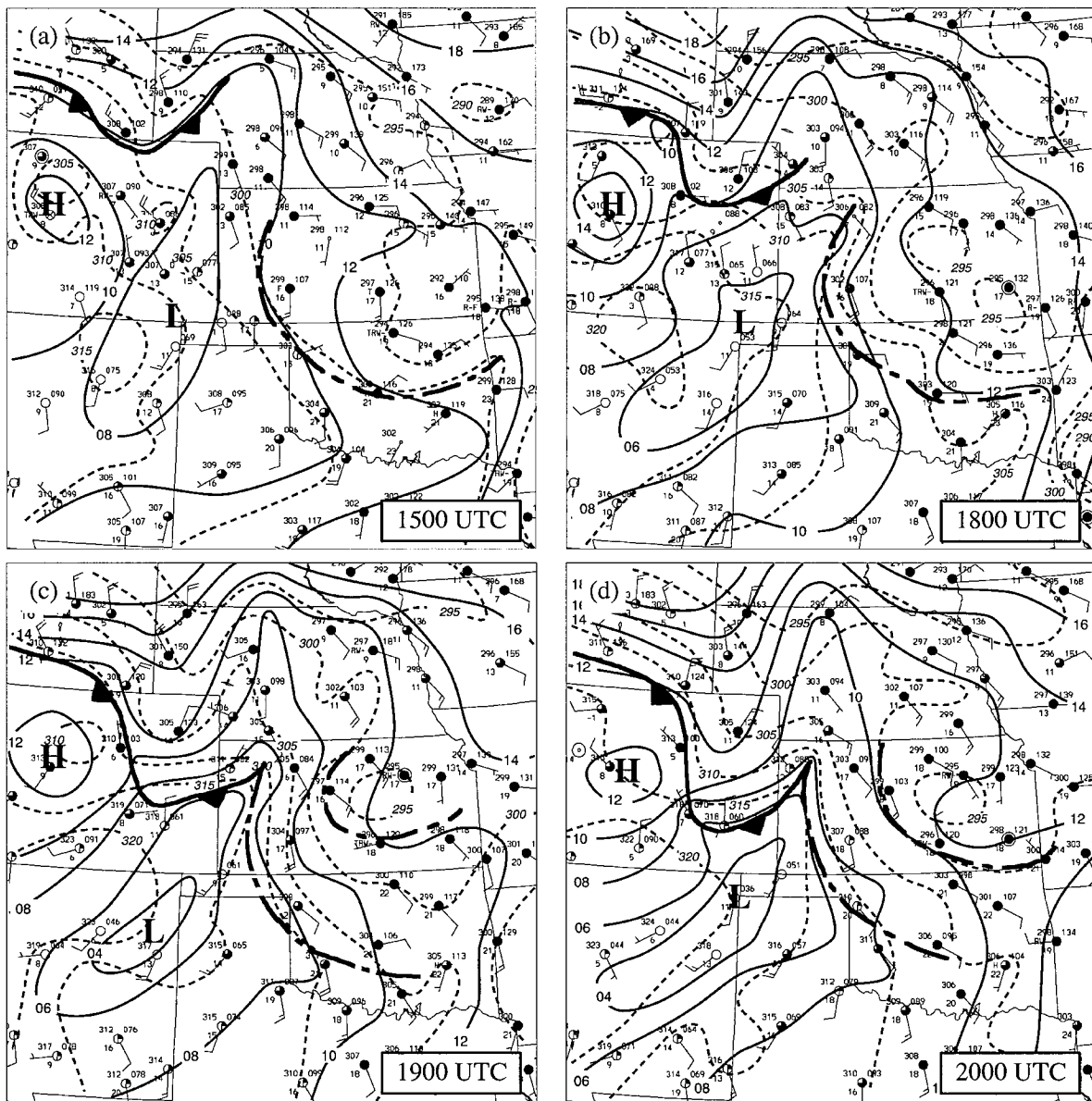


FIG. 3. Surface mesoscale analyses for 10 June 1985. Sea level pressure (solid lines) is contoured at 2-mb intervals and surface potential temperature (dashed lines) is contoured at 5-K intervals. The leading edge of the cold-frontal zone is indicated by the solid barbed line and outflow boundaries by dash-dotted lines. For each station, the potential temperature (K), dewpoint temperature ($^{\circ}\text{C}$), and pressure (divide by 10 and add 1000 to get value in millibars) are indicated in the upper right, lower right, and upper left corners, respectively. Full wind barbs correspond to 5 m s^{-1} and half-barbs to 2.5 m s^{-1} .

showed that after 2100 UTC the intersection of this outflow boundary and the gust front played an important role in the development of a tornadic storm immediately ahead of the squall line.

A visible satellite image at 1930 UTC (Fig. 4a) shows the initial development of the clouds associated with what would become the 10–11 June squall line. Along the Colorado–Kansas border, a cloud band (A) had formed along the leading edge of the potentially cooler air moving southward west of the trough axis. Cloud development B formed along the western edge of the

10 June MCS-produced cold pool and near the trough axis and was located just to the south of cloud band A. Another narrow cloud line (C) was located in southwestern Kansas and extended into northeastern New Mexico (just outside the western edge of the satellite image). It was oriented nearly perpendicular to the MCS cold pool boundary and parallel to the advancing cold front but was located about 160 km ahead of the front within the potentially warmer air in the lee trough. This cloud line evolved into the southern portion of the 10–11 June squall line. Observations (other than satellite

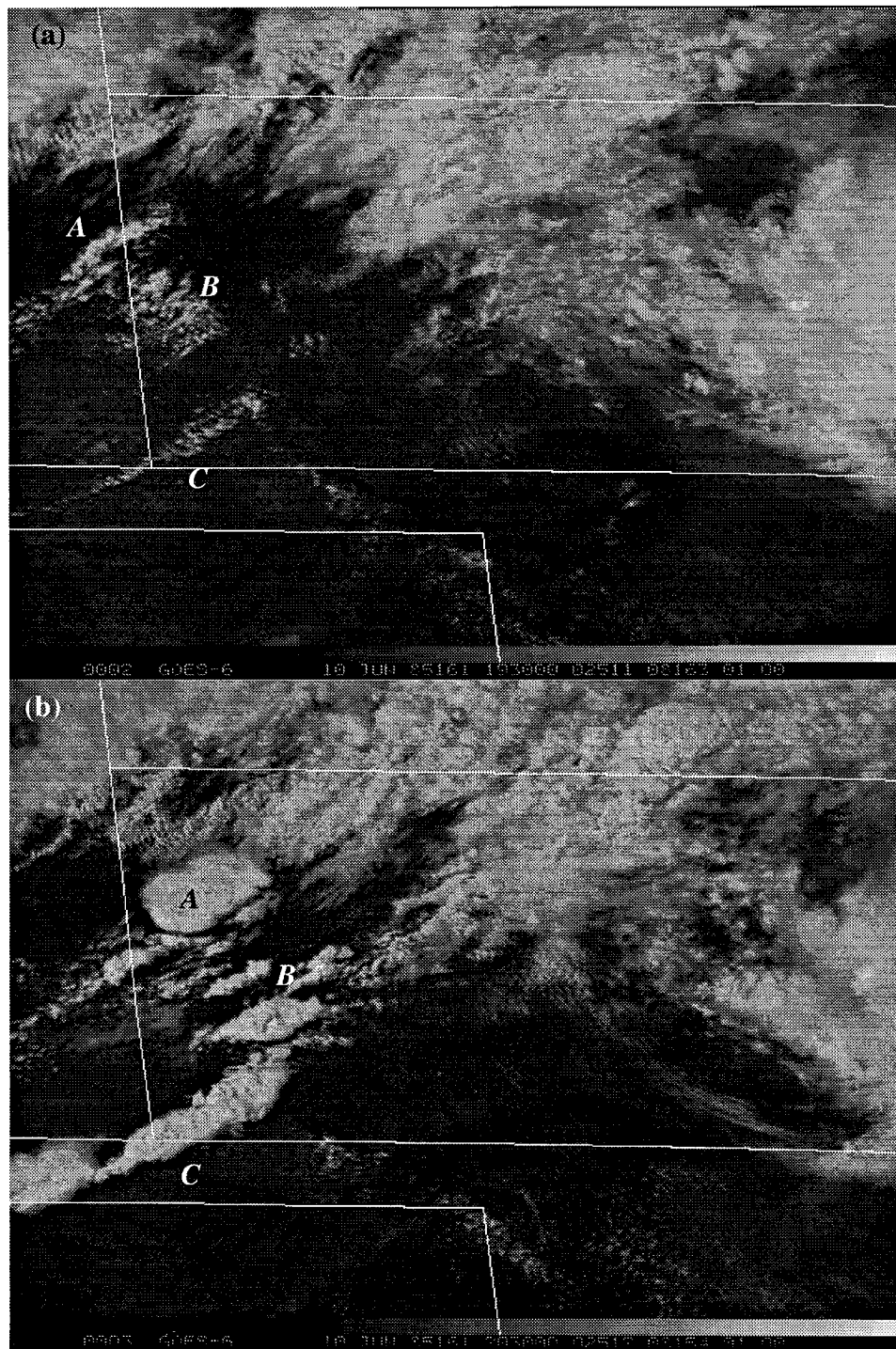


FIG. 4. Visible satellite images for (a) 1930 UTC and (b) 2030 UTC 10 June 1985. The locations of cloud areas A, B, and C are indicated.

pictures) in the region of cloud line C were scarce, but there was no indication of cold air advancing into the region (i.e., no cold front or cold outflow appeared to be associated with the cloud line). However, mesoscale model results from ZGP and those presented herein sug-

gest that convectively produced cold air from central Colorado may have moved into southeastern Colorado and triggered cloud line C near the lee trough axis.

At 2000 UTC, the convective elements that developed into the squall line were apparent in the infrared satellite

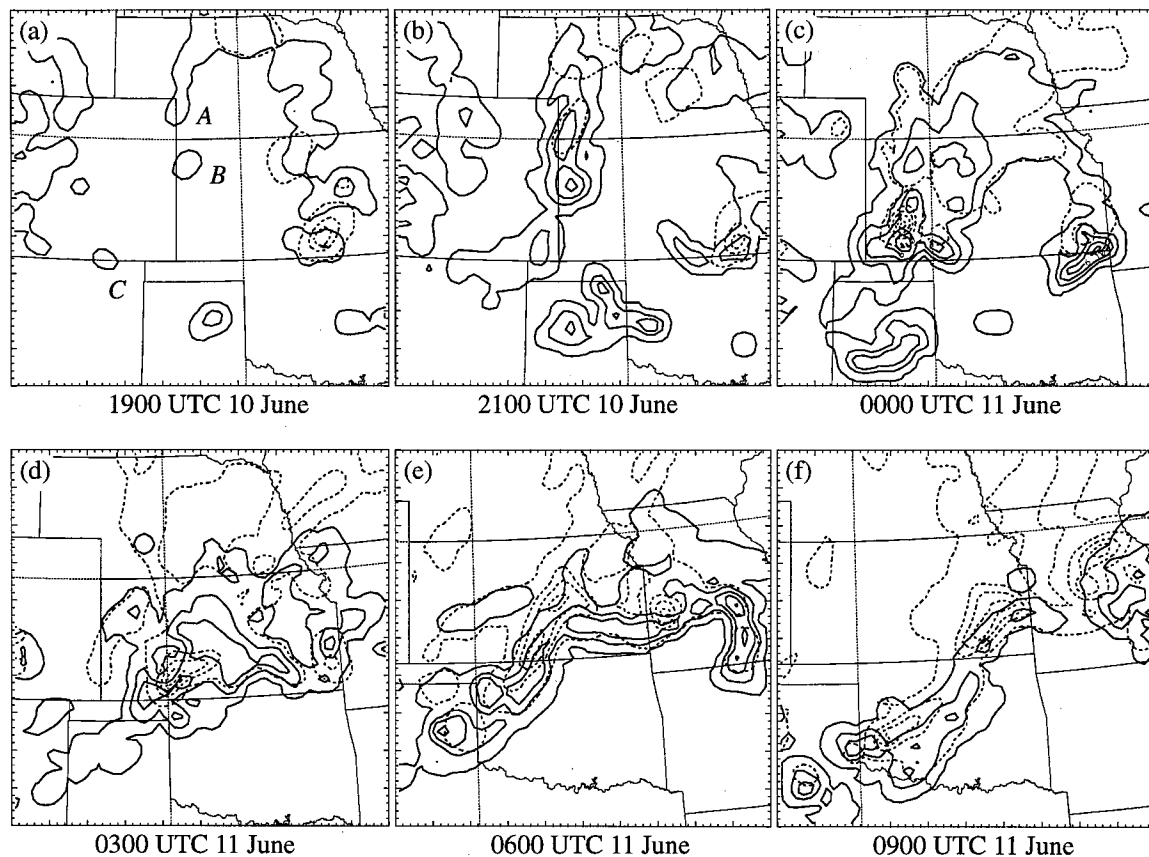


FIG. 5. One-hour parameterized (solid) and grid-resolvable (dashed) rainfall (mm). Contours are drawn at 2-mm intervals for the parameterized rainfall and 4-mm intervals for the explicit rainfall beginning at 0.1 mm. In (a), rain areas A, B, and C are indicated. Axis tick marks are drawn every 20 km.

imagery (not shown). A visible satellite image at 2030 UTC (Fig. 4b), along with the surface analysis at 2000 UTC (Fig. 3d), clearly indicates that these cloud elements were not forced by a single mechanism (i.e., a cold front) but by the three mechanisms described earlier. Cloud A exhibited a nearly circular cloud shield in northwestern Kansas. A cloud line extended southwestward from this cloud shield and was collocated with the leading edge of the cold air in northeast Colorado (Fig. 3d). At 2030 UTC, the cloud elements comprising cloud group B were well separated and appeared loosely organized along the western edge of the cold outflow from the 10 June MCS. However, by 2100 UTC (see Fig. 6a of Johnson and Hamilton 1988), the upper cloud shields of B had merged and had nearly joined with the upper cloud shields associated with cloud areas A and C. Thus, the squall line gradually became a long line of connected convection, but it was not initiated by a single cold-air boundary.

b. Environmental characteristics and model verification

In this section, we describe the mesoscale environment at the time of initiation and verify that the model

captured the initiation of the squall line and the evolution of its precipitation structure. Figure 5 shows the parameterized (solid) and grid-resolvable (dashed) 1-h rainfall amounts for selected times. Plots of the total hourly rainfall (parameterized plus grid-resolvable) corresponding to the times in Figs. 5a and 5d–f are shown in Figs. 8 and 21, respectively. At 1900 UTC (7 h) (Fig. 5a), the parameterized rainfall shows three regions of weak rainfall along the eastern and southern borders of Colorado that in time increase in magnitude and coverage (Figs. 5b and 5c) to form the 10–11 June squall line. The timing of the initiation of these rainfall areas agrees well with the observed time (~ 1930 UTC, Fig. 4a); however, the initial locations of rain areas A and B are shifted northward of the observed locations (ZGP noted a similar displacement in their simulation), causing a gap between rain areas B and C at the initial times.

The cause for the discrepancy in the initial locations of rain areas A and B can be seen in the model sea level pressure and surface potential temperature fields (Fig. 6) valid at 1900 UTC (7 h). The lee trough in the sea level pressure field was reproduced in the simulation; however, the trough axis was located somewhat west-

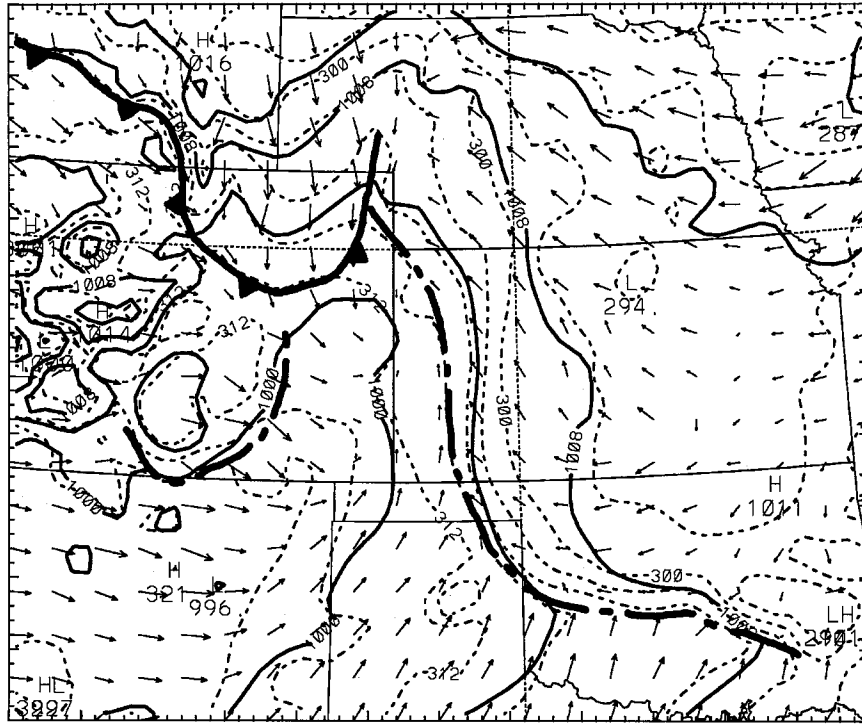


FIG. 6. Sea level pressure and surface potential temperature valid at 1900 UTC 10 June. Sea level pressure (solid) is contoured at 4-mb intervals and potential temperature (dashed) at 3-K intervals. Axis tick marks are drawn every 20 km. Velocity vectors 60 km in length correspond to 15 m s^{-1} . The leading edge of the cold frontal zone is indicated by the solid barbed line and outflow boundaries by dash-dotted lines.

ward of its observed location (Fig. 3a). The cold outflow from the 10 June MCS over central Kansas (Fig. 5a) produced a strong thermal gradient extending from central Oklahoma into southwestern Nebraska. The leading edge of the cold air moving southward into Colorado on the western side of the lee trough was located northward of its observed position (Figs. 3c and 6). This northward displacement of the advancing cold front in the model appears to be the cause of the similar displacement of rain areas A and B (Fig. 5a).

Although their locations are somewhat in error, the mechanisms by which the rain areas formed appear to be consistent with our interpretation of the surface analyses (Fig. 3). Rain area A formed along the leading edge of the cold front and along the intersection of this front with the MCS-generated cold outflow. In northwestern Kansas, rain area B formed at the western edge of the MCS outflow and approximately 100 km ahead of the cold front. This region was characterized by low-level convergence near the center of a weak cyclonic circulation at the surface. Rain area C formed within the warm air near the lee trough axis and along cold outflow from convection over central Colorado. Although such cold outflow was not apparent in the sparse surface observations, the National Weather Service (NWS) radar summary at 2035 UTC (Fig. 7a) indicates that convection was active over south-central Colorado

and thus suggests that cold outflow may have indeed contributed to the formation of cloud line C.

Geopotential height and vector wind fields for 1900 UTC (12 h) at 850 and 500 mb are shown in Fig. 8. At 850 mb (Fig. 8a), the lee trough was strongest adjacent to the terrain over eastern Colorado. The initial squall-line precipitation formed near the trough axis. Northerly mountain-parallel flow developed behind the squall line as the trough extended away from the mountains toward the northeast. At 500 mb (Fig. 8b), the convective clouds were embedded in the westerly flow crossing the mountains. The orientation of the northern portion of the developing line was nearly perpendicular to the flow at 500 mb—a factor that we will see was important in establishing the strength of the rear inflow.

Precipitation associated with the 10 June MCS was located in central Kansas (Fig. 8), in agreement with the radar observations (Fig. 7a). A mesoscale trough and warm-core vortex formed at midlevels in association with this MCS (Fig. 8b). Such mesoscale vorticity centers are occasionally seen in satellite data as spiral-shaped midlevel cloud patterns in decaying MCSs (Bartels and Maddox 1991; Johnson and Bartels 1992; Fritsch et al. 1994) and may aid the longevity of MCSs or cause the development of new MCSs downstream (Bosart and Sanders 1981; Zhang and Fritsch 1987,



FIG. 7. National Weather Service radar summaries for (a) 2035 UTC 10 June, (b) 0035 UTC 11 June, (c) 0335 UTC 11 June, and (d) 0435 UTC 11 June 1985. Shading levels indicate increasing precipitation intensities.

1988; Raymond and Jiang 1990; Davis and Weisman 1994; Fritsch et al. 1994).

In the model, convection formed over the Texas panhandle and drifted southward (Figs. 5a–c). This convection was not observed and was an artifact of the convective parameterization. It produced a marked cold pool in the surface temperature field of the model and seems to have thus led to an apparent underprediction of the rainfall associated with the 10–11 June squall line over the Texas panhandle (compare Figs. 5b–d with Figs. 7b–d). However, it did not appear to affect significantly the development of the rest of the 10–11 June squall line.

Comparison of the model squall line (Fig. 5) with radar data (Fig. 7) shows that the model squall line moved and developed more slowly than the observed storm. This result may be due to our use of the full precipitation terminal velocity (Weisman et al. 1997). Prior to 2100 UTC (9 h), the model rainfall resulted primarily from the convective parameterization (Figs. 5a,b), and the eastward advancement of the squall line was slow. By 0000 UTC (12 h) 11 June, significant grid-resolvable precipitation began. Subsequently, the squall line moved at a rate comparable to the observed speed of the storm (13 m s^{-1} in the model versus the observed speed of 14 m s^{-1}). In other words, the more

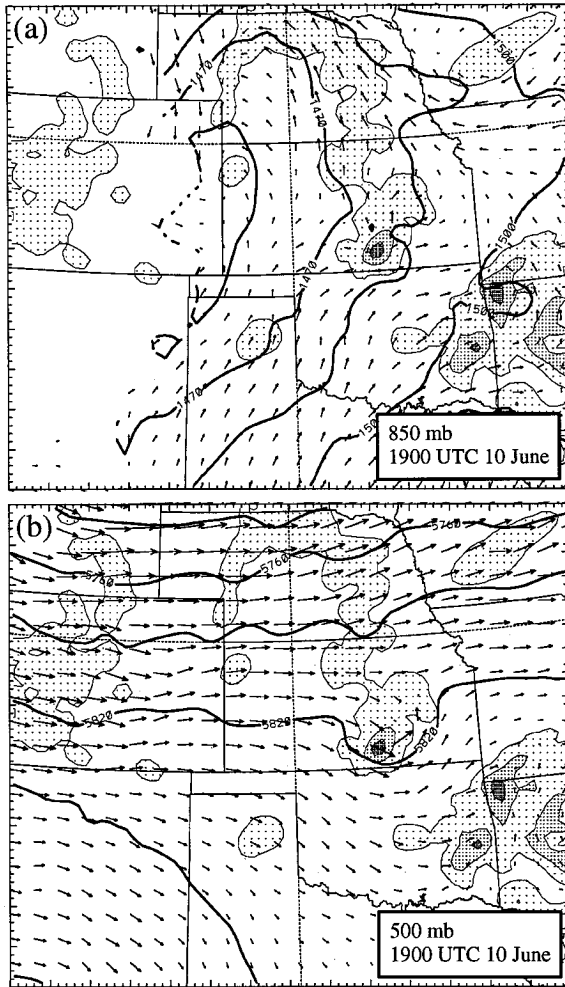


FIG. 8. Geopotential heights, total 1-h rainfall (parameterized and grid-resolvable), and vector winds at 1900 UTC (7 h) 10 June 1985. Heights are contoured at 15-m intervals at 850 mb and 30 m at 500 mb. In (a) contours and vectors end where the pressure level intersects the terrain. Shading levels correspond to rainfall depths of 0.1, 5, and 10 mm. Axis tick marks are drawn every 20 km. Velocity vectors 60 km in length correspond to 20 m s^{-1} .

accurate movement and evolution of the squall line did not occur until the vertical circulation and precipitation processes of the squall line became resolvable on the fine mesh. Consequently, at 2100 UTC and later times, the modeled squall line was located to the west of its observed location and did not begin to decay until about 2 h after the observed storm (~ 0800 UTC versus 0600 UTC). Although the model squall line evolved more slowly than the observed one, its precipitation structure, and that of the precipitation preceding it in eastern Kansas and Missouri, closely resembled the precipitation pattern observed by radar. Therefore, in the discussion that follows, we focus on the evolution of the precipitation structures by comparing the modeled and observed storms at equivalent stages of their evolution rather than at specific times.

At 0300 UTC (15 h) (Fig. 5d), the position and structure of the squall line and the remnant convection of the 10 June MCS in the simulation resembles that seen by radar at 0035 UTC (Fig. 7b). Convective precipitation extended from the Texas panhandle into north-central Kansas, with lighter (grid resolvable) precipitation extending into southeastern Nebraska and Iowa. Precipitation associated with the decaying 10 June MCS was located near the eastern Kansas border.

At 0600 UTC (18 h) (Fig. 5e), the model storm is similar to the observed storm at 0335 and 0435 UTC (Figs. 7c,d). The large area of resolvable precipitation that developed in the northern and central portions of the 10–11 June squall line is in good agreement with the location of enhanced stratiform precipitation observed by the Wichita radar (see Fig. 2 of Braun and Houze 1994) during the mature stage. Significant parameterized and grid-resolved precipitation developed in Missouri and a rainband extended westward to the northern portion of the 10–11 June storm. A similar pattern is seen in the radar observations. This rainband was apparently produced by the convergence of northeastward flow around the incipient cyclone over Missouri and the southerly flow ahead of the 10–11 June squall line (see Fig. 21). These results indicate that while the timing of the simulated storm may be too slow, the observed precipitation structure is reasonably reproduced.

At 0900 UTC (21 h) (Fig. 5f), the parameterized convection weakened and the resolvable precipitation split into two cores. A similar split was observed near 0700 UTC in satellite and radar data (see Figs. 2 and 3 in Rutledge et al. 1988) and occurred where the rear inflow was maximum. Section 4c shows that this region of maximum rear inflow was strongly influenced by microphysical processes.

4. Effects of the large-scale environment and cloud microphysics on the mesoscale airflow of the squall line

a. Observed airflow and precipitation structure from dual-Doppler radar

The reflectivity and storm-relative airflow structure as revealed by the composite dual-Doppler radar data of Biggerstaff and Houze (1993) at 3.4 km (approximately 0.5 km below the 0°C level) is shown in Fig. 9. This dataset was derived from a composite of 11 dual-Doppler syntheses over the period 0130–0530 UTC. Although no information is available from the composite fields on the evolution of the rear inflow, the composite fields describe well some of the important steady features of the circulations. The coordinate system has been rotated such that the north–south axis is turned counterclockwise by 35° . The composite radar analysis covers the northern portion of the squall line and extends from the north end of a bow echo ($y = 0$

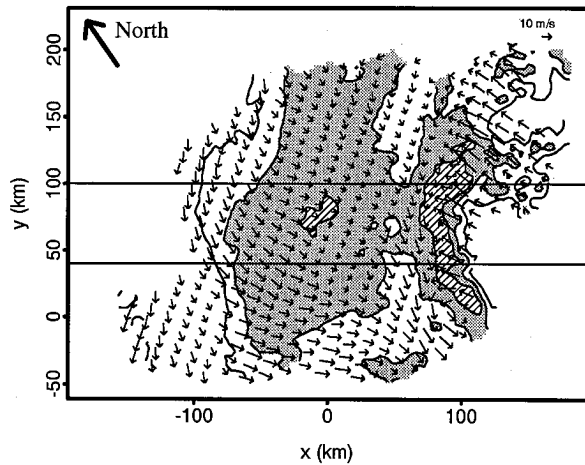


FIG. 9. Radar reflectivity (dBZ) and storm-relative wind vectors at 3.4 km. Reflectivity is contoured at 15, 30, and 40 dBZ. Shading indicates reflectivities between 30 and 40 dBZ and hatching indicates values greater than 40 dBZ. The vector wind scale is indicated in the upper-right corner. The horizontal lines enclose the 60-km-wide region over which the along-line averaging is performed.

km) to the north end of the solid (i.e., unbroken) part of the convective line. The leading convective line is located between $x = 60$ and 120 km. A secondary maximum in radar reflectivity, or secondary band, is seen within the trailing stratiform region between $x = -80$ and 40 km. Located between the convective line and the secondary band is a narrow zone of minimum radar reflectivity, often referred to as the reflectivity trough or transition zone. Braun and Houze (1994) analyzed the secondary band and transition zone in detail. The airflow within the stratiform region at this level was generally northerly to northwesterly and associated with descending rear inflow. Vertical cross sections (Fig. 10) oriented normal to the squall line were obtained by averaging over a 60-km-wide strip oriented perpendicular to the line (Fig. 9). The fields in these mean cross sections are identical to those discussed in Biggerstaff and Houze (1993) except that they are displayed in pressure coordinates and the horizontal axis has been compressed to facilitate comparison with model fields in sections 4b and 4c(2). The mean reflectivity field (Fig. 10a) was characterized by a 60-km-wide leading convective line, followed by a nearly 150-km-wide region of stratiform precipitation.

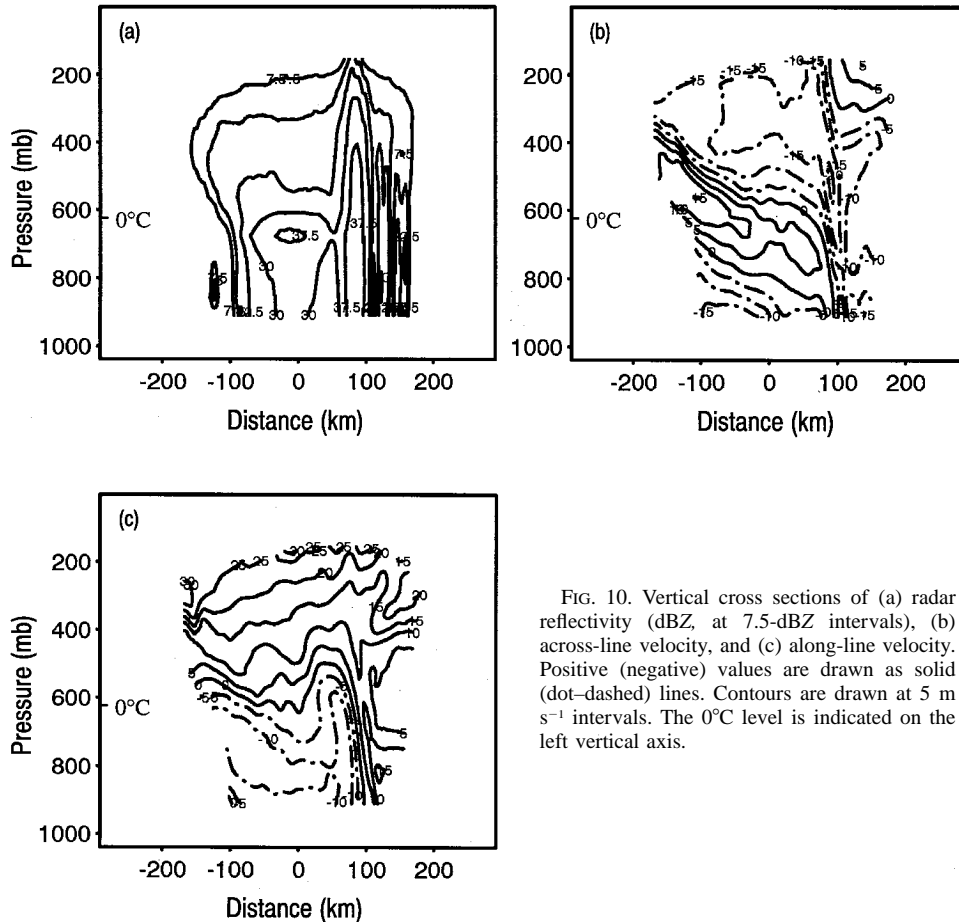


FIG. 10. Vertical cross sections of (a) radar reflectivity (dBZ, at 7.5-dBZ intervals), (b) across-line velocity, and (c) along-line velocity. Positive (negative) values are drawn as solid (dot-dashed) lines. Contours are drawn at 5 m s^{-1} intervals. The 0°C level is indicated on the left vertical axis.

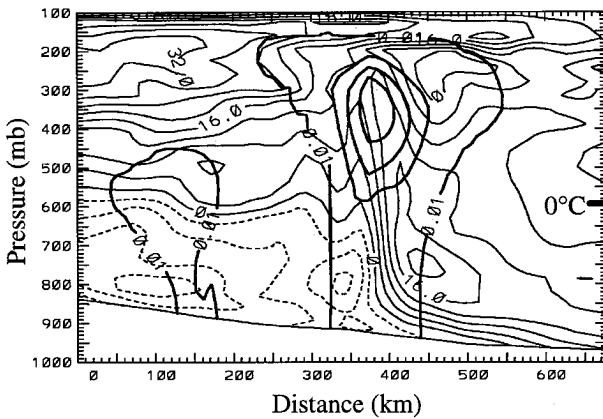


FIG. 11. Vertical cross section of the precipitation mixing ratios (thick solid lines) and along-line velocity component at 0300 UTC (15 h) 11 June 1985. The location of the cross section is shown in Fig. 12a. Precipitation mixing ratio contours are drawn at 2 g kg^{-1} intervals starting at 0.01 g kg^{-1} . Along-line velocity is contoured at 4 m s^{-1} intervals with positive values (solid lines) corresponding to flow into the page. The 0°C level is indicated on the right vertical axis.

The across-line velocity field (Fig. 10b) shows FTR flow entering the convective region between the surface and 300 mb (10 km). The boundary layer air rose sharply and the velocity achieved maximum strength within the convective region. The base of this FTR flow remained above about 500 mb (5.5 km) in the trailing stratiform region. A layer of RTF velocity occurred near the melting level ($\sim 625 \text{ mb}$) in the stratiform rain region. It dropped to near the surface in the convective region. A relative maximum of RTF flow occurred between the convective line and the secondary maximum of radar reflectivity in the stratiform region ($0 < x < 100 \text{ km}$). The strongest RTF flow occurred at the back edge of the stratiform precipitation region and beneath the overhanging layer of precipitating ice where strong sublimative cooling took place (Rutledge et al. 1988; Stensrud et al. 1991). This maximum rear inflow was consistently about twice as strong as the RTF flow behind the convective line (see Fig. 11 of Smull and Houze 1987 and Figs. 5–7 of Rutledge et al. 1988). It is primarily the mesoscale portion of the rear inflow located at $x < 0 \text{ km}$ to which we compare the mesoscale model results rather than the smaller-scale internal circulation structures ($0 < x < 120 \text{ km}$) since the resolution of the mesoscale model is insufficient to resolve these internal structures well.

The along-line velocity field (Fig. 10c) shows northeasterly (out of page) flow below the melting level in the stratiform region. Behind the convective line, the northeasterly flow extended upward to near 6 km and was somewhat more intense than within the stratiform region. Strong horizontal shear occurred within the convective line where southwesterly (into page) inflow transitioned to northeasterly flow behind the gust front.

Strong vertical wind shear occurred to the rear of the convective region.

b. Evolution of the along-line flow in the mesoscale model

As was shown in Fig. 8, the squall line formed near or along the trough axis at low levels (surface to about 700 mb). This juxtaposition of the squall line and trough largely explains the distribution of along-line velocity seen in the radar analysis (Fig. 10c) and calculated in the simulation (Fig. 11). The velocity pattern in Fig. 11 indicates that the northeasterly flow observed within the squall-line system (Fig. 10c) was part of a larger-scale circulation in which the squall line was embedded. At 0300 UTC (15 h) (Fig. 12), a trough at 800 mb extended from near the mountains in New Mexico toward the northeast. The squall line was oriented along the trough and located on its northwestern side. The flow ahead of the squall line was directed from the south to southwest, while behind the line the flow was from the north and northeast. A sharp transition from northeasterly to southwesterly flow thus occurred across the squall line. This juxtaposition of the squall line and trough produced the northeasterly storm-relative along-line flow behind the squall line. West-northwesterly flow at 500 mb (Fig. 12b) indicates a layer of transition from northeasterly along-line flow at low levels to southwesterly along-line flow at higher levels (Figs. 10c and 11). These upper-level analyses suggest that a significant portion of the along-line flow was attributable to the larger-scale environment of the squall line. Gao et al. (1990) discuss how this larger-scale along-line flow was modified by the squall line.

c. Evolution of the across-line flow in the mesoscale model

1) DEVELOPMENT AND HORIZONTAL VARIABILITY OF REAR INFLOW

Figures 8b and 12b show the squall line oriented nearly perpendicular to the flow near 500 mb with strong west-to-west-northwesterly flow behind the squall line. In this section, we demonstrate how this west-northwesterly flow interacted with the squall line to produce the strong mesoscale rear inflow observed along the central portion of the line.

Figure 13 shows the evolution of the RTF flow at 500 mb at 2-h intervals beginning just prior to the formation of strong rear inflow. The shading indicates the resolvable-scale snow mixing ratios, and the vectors show the storm-relative flow [storm motion of 13 m s^{-1} from 303.5° based on the motion of the surface rainfall band (section 3b, Fig. 5)]. The thick solid straight lines show the locations of vertical cross sections [section 4c(2)]. These cross sections lie along a fixed vertical plane oriented in the direction of storm motion. Each equal-length

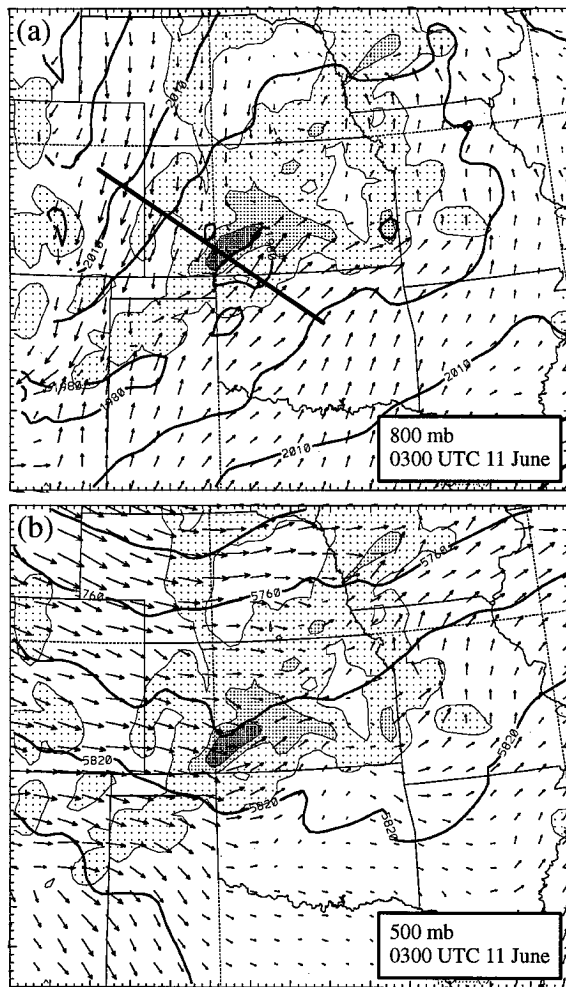


FIG. 12. Geopotential heights, total 1-h rainfall (parameterized and grid-resolvable), and vector winds at 0300 UTC (15 h) 11 June 1985. Heights are contoured at 15-m intervals at 800 mb and 30 m at 500 mb. In (a) contours and vectors end where the pressure level intersects the terrain. Shading levels correspond to rainfall depths of 0.1, 5, and 10 mm. Axis tick marks are drawn every 20 km. Velocity vectors 60 km in length correspond to 20 m s^{-1} . Thick line in (a) indicates location of cross section (Fig. 11).

line represents a different segment of this plane such that the squall line remains centered in the vertical cross section. The contours in Fig. 13 give the magnitude of the across-line component of the storm-relative flow (i.e., the component parallel to the cross sections). Bold contours indicate RTF flow exceeding 8 m s^{-1} .

At 0200 UTC (14 h) (Fig. 13a), RTF flow dominated the region behind the squall line and a narrow band of enhanced RTF flow existed along the rear (western) edge of the squall line. By 0300 UTC (not shown), the RTF flow magnitude had nearly doubled in a small region immediately behind the area of largest snow mixing ratios. This RTF flow had intensified farther by 0400 UTC (Fig. 13b) but then weakened slightly or remained relatively steady (Fig. 13c) until it reintensified at 0800

UTC (Fig. 13d). It was at this time, when the rear inflow was reintensifying, that the splitting of the resolvable-scale precipitation occurred (Fig. 5f). The along-line horizontal scale of the rear-inflow core, approximately 100–200 km, was similar to the horizontal scale of the maximum in snow mixing ratios along the central portion of the line and remained relatively constant after 0400 UTC.

A secondary maximum of snow mixing ratios formed along the northern portion of the squall line by 0600 UTC (18 h) (Fig. 13c). The magnitude of the rear inflow to the rear of this maximum was weak. By 0800 UTC (Fig. 13d), however, a small core of rear inflow exceeding 4 m s^{-1} formed immediately to the rear of the secondary snow maximum. Similar to the primary rear-inflow core, this secondary core of rear inflow possessed an along-line horizontal scale comparable to the scale of the snow maximum.

The evolution of the rear inflow seen in Fig. 13 shows that the rear-inflow cores were closely associated with the maxima of snow mixing ratios aloft, which were, in turn, associated with the strongest updrafts. The formation of the rear-inflow cores lagged that of the snow maxima by up to 2 h (e.g., in the northern portion of the squall line in Figs. 13c,d). The occurrence of the primary maximum in snow mixing ratios, and rear inflow, along the central portion of the line agrees with the low-level composite radar structure in Biggerstaff and Houze (1991a), which showed the heaviest precipitation to be associated with a bow echo along the central portion of the squall line. The core of rear inflow also accounts for the notch that later developed in the low-level radar reflectivity at the rear of the stratiform region along the central portion of the storm (Rutledge et al. 1988; Johnson and Hamilton 1988). The snow mixing ratio maximum along the central portion of the line is also consistent with the findings of Houze et al. (1990) and Skamarock et al. (1994) that mature squall lines with symmetric organization (i.e., stratiform precipitation distributed nearly uniformly behind the convective line) often have the strongest convection near the center of the convective line. The association of the rear-inflow core with the maximum snow mixing ratios agrees qualitatively with dual-Doppler analyses, which show the strongest RTF flow rearward of the most intense reflectivity cores (Klimowski 1994).

Figure 14 shows geopotential heights at 500 mb and buoyancy at 400 and 600 mb at 0400 and 0800 UTC (16 and 20 h), which correspond to the times in Figs. 13b and 13d. The buoyancy includes the perturbation virtual potential temperature and the hydrometeor water loading. The perturbation virtual potential temperature was determined by subtracting a pressure-level mean value determined for the areas represented in Fig. 14. At 0200 UTC (14 h) (not shown), when the RTF flow was strengthening in a narrow band at the back edge of the squall line (Fig. 13a), a mesoscale trough was evident in the region immediately behind the maximum

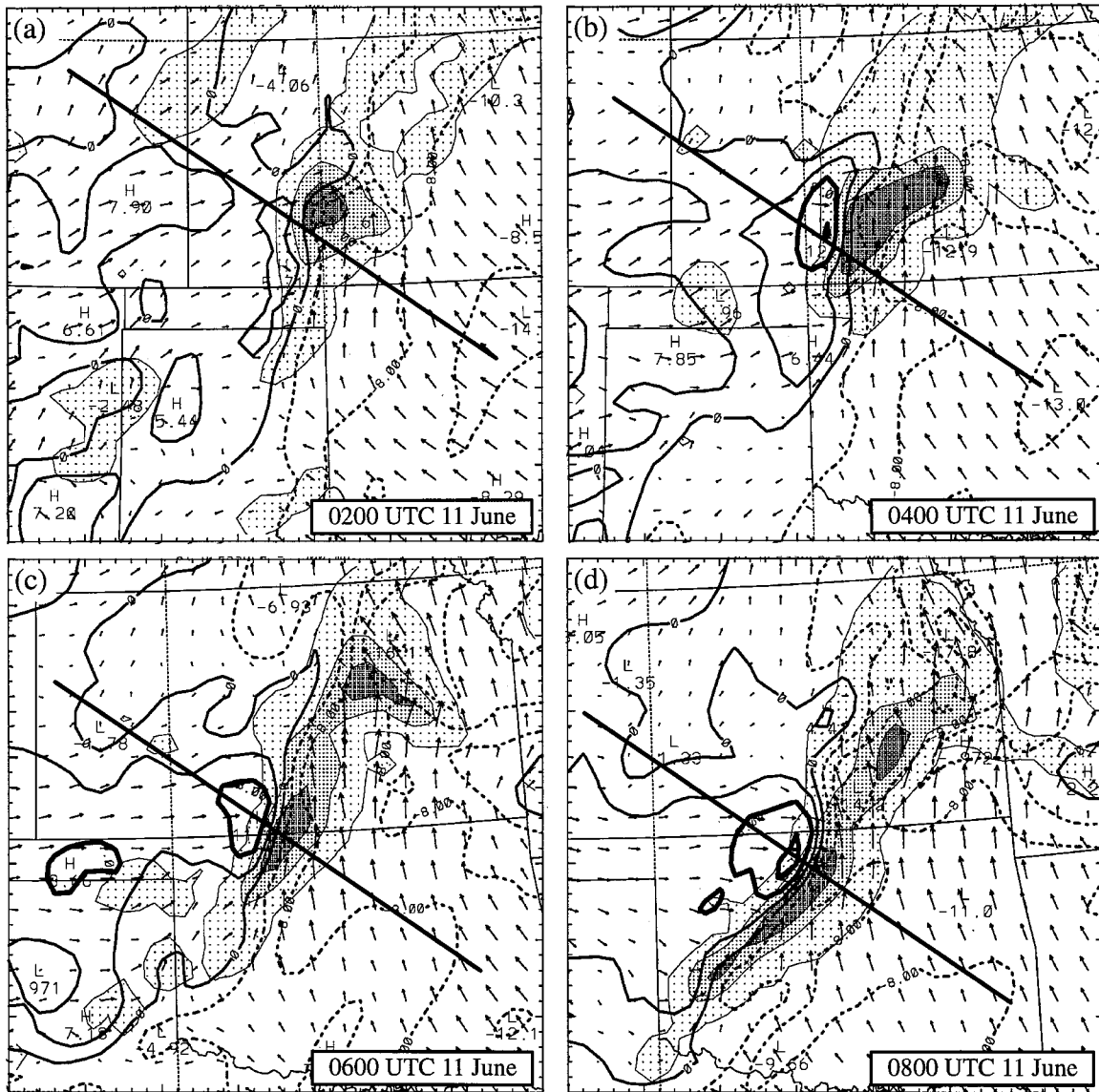


FIG. 13. Snow mixing ratios (shading), across-line velocity (contours), and storm-relative velocity vectors at 500 mb. Shading levels correspond to snow mixing ratios of 0.1, 2, and 4 g kg^{-1} . Contours show the magnitude of the storm-relative flow in the direction of storm motion (i.e., parallel to the thick solid lines, which show the locations of cross sections in Figs. 17–20) at 4 m s^{-1} intervals. Solid (dashed) contours correspond to RTF (FTR) flow. Bold contours indicate RTF flow exceeding 8 m s^{-1} . Axis tick marks are drawn every 20 km. Velocity vectors 40 km in length correspond to 20 m s^{-1} .

snow mixing ratios. The trough produced accelerations that led to the initial development of the core of maximum RTF flow. By 0400 UTC (Figs. 14a,b), the mesotrough amplified and extended farther southwestward along the line. The most intense RTF height gradients and RTF flow were at the back edge of the maximum snow mixing ratios. The buoyancy field at 400 mb shows a positive anomaly associated with the convective system. The mesotrough and rear-inflow core at 500 mb were located beneath a portion of the region of strong buoyancy gradient at 400 mb. The buoyancy field at 600 mb indicates a negative anomaly coincident with

the 500-mb mesotrough and a small-scale region of strong buoyancy gradient (of a sign opposite to that at 400 mb) collocated with the rear-inflow core. The regions of positive (negative) across-line buoyancy gradient at 400 (600) mb correspond to regions of negative (positive) horizontal along-line vorticity generation and apparently contributed to the rear inflow in the manner depicted in Fig. 15 (from Weisman 1992). The negative buoyancy anomaly at 600 mb was associated with latent cooling, primarily as a result of sublimation since the 600-mb level was slightly above the 0°C level within this portion of the squall line.

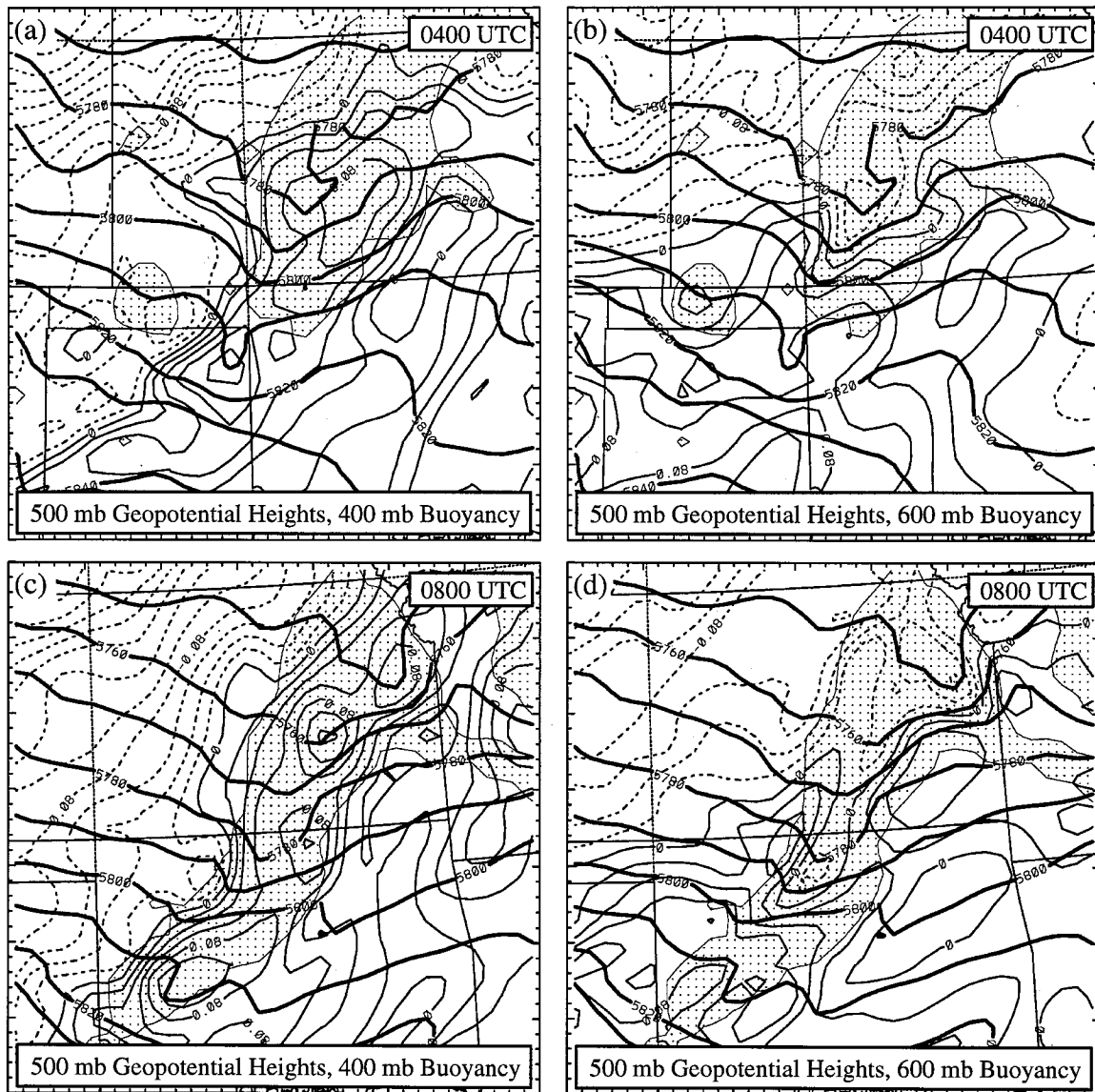


FIG. 14. Geopotential heights at 500 mb (bold contours) and buoyancy at 400 mb (a, c) and 600 mb (b, d). Shading corresponds to snow mixing ratios greater than 0.1 g kg^{-1} , as in Figs. 13b,d. Height contours are drawn at 10-m intervals and buoyancy contours at 0.02 m s^{-2} intervals. Axis tick marks are drawn every 20 km.

By 0600 UTC (not shown), when the secondary maximum of snow formed in the northern portion of the squall line, an enhancement of the mesotrough was evident rearward of this snow maximum that eventually led to the secondary core of rear inflow at 0800 UTC (Fig. 13d). By 0800 UTC (Figs. 14c,d), a well-defined trough extended along the length of the squall line. The 400-mb buoyancy field continues to show that the 500-mb mesotrough and rear-inflow core were beneath the 400-mb buoyancy gradient along the back edge of the squall line. A negative buoyancy anomaly was located at the back edge of the system in northern Oklahoma near the region where the squall line's precipitation and cloud shield split during the dissipative stage

of the system. At 600 mb, a negative buoyancy anomaly was still coincident with the 500-mb mesotrough while a positive anomaly, associated with adiabatic warming in the descending rear inflow, was northwest of the negative anomaly. The region of strong buoyancy gradient between these anomalies was well correlated with the rear-inflow core.

The mesoscale model results in Figs. 13 and 14 are consistent with higher resolution modeling studies (Lafore and Moncrieff 1989; Weisman 1992; Skamarock et al. 1994) in that the development of the rear inflow was associated with regions of convectively generated buoyancy gradients. The buoyancy gradient at 400 mb occurred along the entire length of the squall line and was,

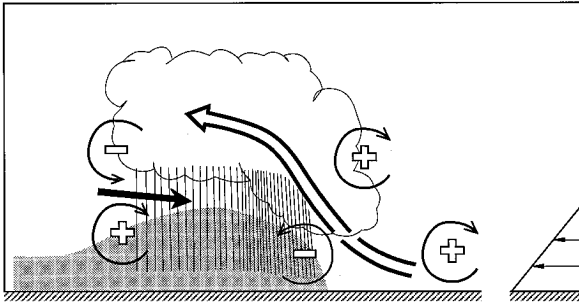


FIG. 15. Conceptual model of the mature stage of an upshear-tilted squall-line-type convective system. The updraft current is denoted by the thick, double-lined flow vector with the rear-inflow current denoted by the thick solid vector. The shading denotes the surface cold pool. The thin circular arrows depict the most significant sources of horizontal vorticity, which are either associated with the ambient vertical wind shear or are generated by horizontal buoyancy gradients within the convective system. Regions of lighter or heavier precipitation are indicated by the more sparsely or densely packed vertical lines, respectively. The scalloped line denotes the outline of the cloud. Adapted from Weisman (1992).

in general, well correlated with the broad region of RTF flow extending along the back edge of the system. In contrast, the region of strong buoyancy gradient behind the negative buoyancy anomaly at 600 mb was much smaller in scale. The scale of this region of strong buoyancy gradient was essentially the same as that of the rear-inflow core. Rutledge et al. (1988) suggested that the strong rear inflow in this storm was associated with sublimative cooling. ZG and Yang and Houze (1995) have shown by numerical experimentation with mesoscale and convective-scale models, respectively, that the maximum of rear inflow at the back edge of the stratiform precipitation region was associated with ice microphysical processes and latent cooling.

While the mesoscale model results suggest a strong association between the rear-inflow core and sublimative cooling, additional evidence is needed to support a contention of cause and effect. Figure 16 shows time series of the maximum cooling rates and rear inflow strength along the back edge of the squall line at 500 and 600 mb for the period 0115–0500 UTC (13.25–17 h). At each level, the cooling rates increased sharply after 0100 UTC. The development of strong sublimative cooling preceded the intensification of the rear inflow by approximately 45 min to 1 h in the 500–600-mb layer. As the rear inflow strengthened, the cooling rates remained relatively steady. These results suggest that sublimative cooling likely contributed to the formation of the rear-inflow core, but the development of the rear inflow did not *subsequently* enhance the sublimative cooling rates at midlevels; however, the maximum cooling coincided with the rear-inflow core. Additional discussion of the effects of sublimative cooling are presented in section 4c(3).

Skamarock et al. (1994), based on high-resolution, three-dimensional simulations of squall lines, associated

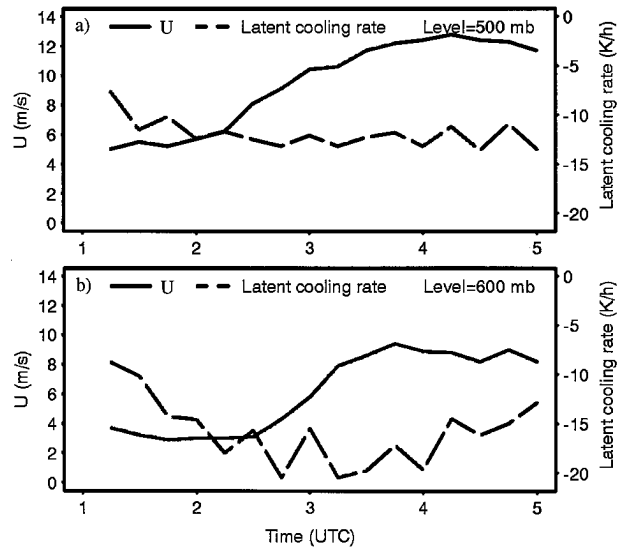


FIG. 16. Time series of maximum rear-inflow strength (U , solid lines) and resolvable-scale latent cooling rate (dashed lines) at (a) 500 and (b) 600 mb during the developing stages of the rear inflow.

the development of strong convection and rear inflow along the central portion of the squall line with circulations at the ends of the squall line. Such line-end effects were probably important in this case. In addition to producing the strongest ascent (and hydrometeor production) along the central portion of the line, the line-end effects may have drawn the ambient RTF flow into the central portion of the storm such that the sublimative cooling and subsequent enhancement of the RTF flow became concentrated there. The mesoscale model results suggest that the effects of the line ends, the ambient RTF flow behind the system, and the sublimative cooling combined to produce the core of strong rear inflow in this case.

Previously, it was noted that the scale of the negative buoyancy anomaly at 600 mb had a horizontal scale similar to the rear-inflow core and mesotrough at 500 mb. One could speculate that the scale of the rear-inflow core was determined by the scale of the sublimation-induced negative buoyancy anomaly. On the other hand, one could argue that the scale of the negative buoyancy anomaly was determined by the scale of the rear-inflow core since the strongest sublimation was collocated with this core. A more plausible explanation is that neither feature determined the scale of the other but that the scales of both were determined by line-end effects, while the strength of the rear-inflow core was influenced by the ambient RTF flow and the sublimative cooling.

ZGP and ZG suggested that a midlevel mesoscale cyclonic vortex in the northern portion of the stratiform region assisted the development of rear inflow along the central portion of the line since the strongest rear inflow was southwest of the vortex. However, this vortex, initially associated with the midlevel short-wave trough and then enhanced by the squall line, generally lay be-

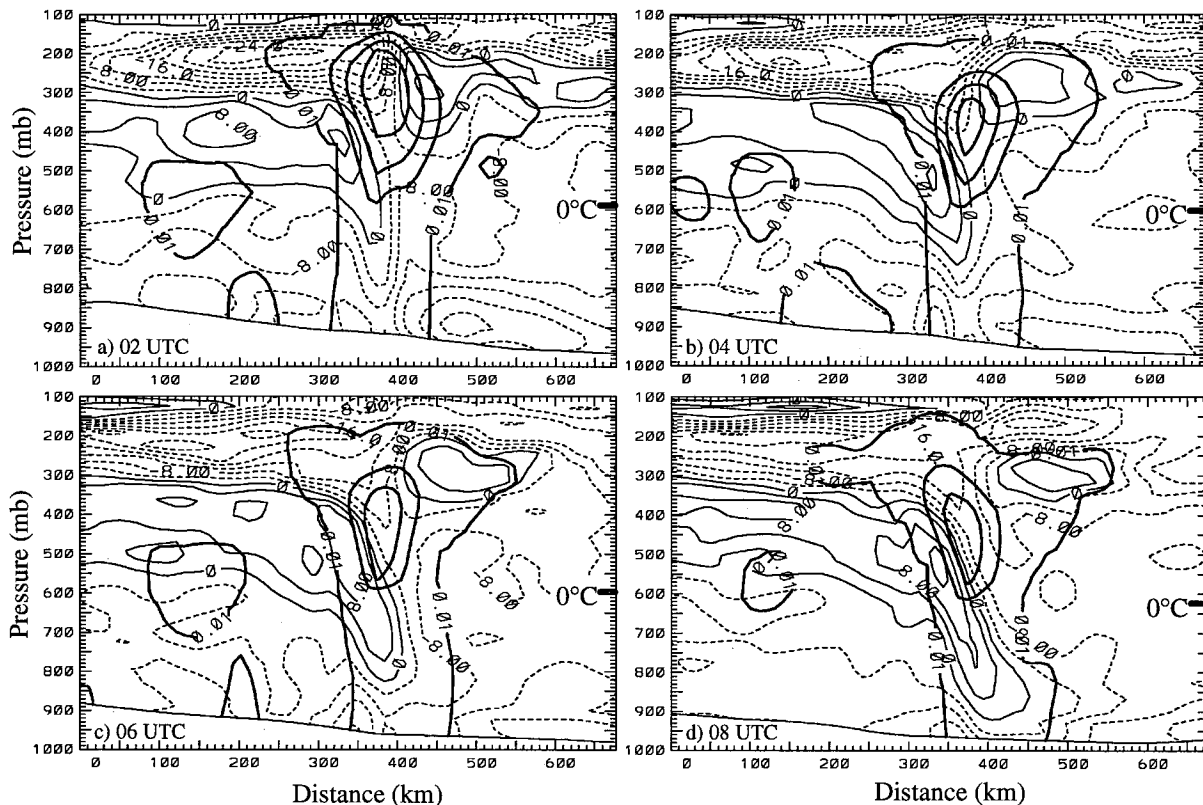


FIG. 17. Vertical cross sections of precipitation mixing ratios (thick solid lines) and across-line storm-relative velocity component at 2-h intervals on 11 June 1985. The locations of the cross sections are shown in Fig. 13. Precipitation mixing ratio contours are drawn at 2 g kg^{-1} intervals starting at 0.01 g kg^{-1} . Across-line velocity is contoured at 4 m s^{-1} intervals. Solid (dashed) lines correspond to RTF (FTR) flow. The 0°C level in the presquall environment is indicated on the right vertical axis.

low the core of strongest rear inflow (ZG; Biggerstaff and Houze 1991b; Zhang 1992). The storm-relative winds and across-line velocities in Fig. 13, combined with the 500-mb heights and 400- and 600-mb buoyancy fields in Fig. 14, suggest that the formation of the rear-inflow core along the central part of the line occurred not as a direct result of the mesoscale vortex but primarily in response to buoyancy gradients associated with warming in strong ascent along the central part of the line and sublimative cooling at the back edge of the system during the early-to-mature stages of the squall line. The differences in our findings and those of ZGP and ZG arise more from differences in the interpretation of the simulation results rather than from actual differences in the simulations.

2) EVOLUTION OF THE VERTICAL STRUCTURE OF THE REAR INFLOW

The evolution of the vertical structure of the rear inflow is illustrated by Fig. 17, which shows cross sections (located along the thick solid lines in Fig. 13) of the precipitation mixing ratios and the across-line component of the storm-relative flow. Figures 18–20 show corresponding cross sections of vertical p -velocity ω and

perturbations of potential temperature θ' and geopotential height z' . The θ' and z' fields were obtained by subtracting mean profiles of θ and z determined by averaging θ and z at the leading edge of hourly cross sections (of which half are shown in Fig. 13) over the period 0100–0800 UTC. By removing the mean values at the leading edge, the contoured values represent perturbations from mean presquall environmental values, which is similar to the representation of potential temperature and pressure fields often shown in cloud modeling and thermodynamic retrieval studies. Since the θ' and z' fields are perturbations with respect to values at the leading edge of the cross sections, the large-scale ridge ahead of the squall line causes the convectively generated upper-tropospheric warming (Fig. 19) and mesohigh (Fig. 20) to appear weak.

The ability of the mesoscale model to simulate features of the squall line's circulations is limited by the horizontal resolution (20-km grid spacing). Figure 17 indicates that the RTF flow gradually descended, reaching low levels near the leading edge of the line by 0800 UTC (20 h) (Fig. 17d). However, Doppler radar observations showed that RTF flow extended into the convective region by early stages of the storm (Fig. 4 of Rutledge et al. 1988). Comparison of Fig. 17 to Fig. 3

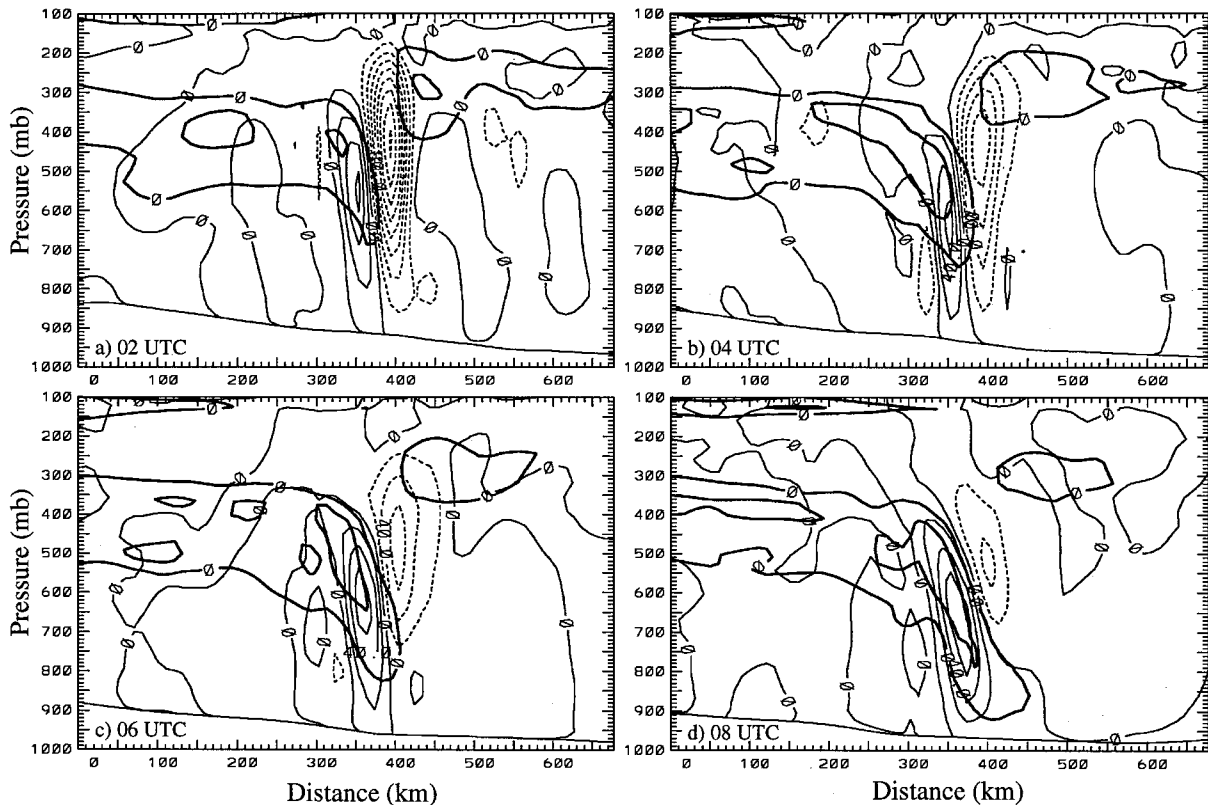


FIG. 18. Vertical cross sections of vertical motion ω at intervals of $20 \mu\text{b s}^{-1}$ on 11 June 1985. Dashed (solid) lines indicate upward (downward) motion. Heavy solid lines are contours of RTF velocities at 0 and 8 m s^{-1} .

in Gallus and Johnson (1991) shows reasonable agreement between the evolution of the mesoscale flows. Unlike some observed squall lines that exhibit little or no RTF flow across the back edge of the stratiform region (Chong et al. 1987), the 10–11 June storm was characterized by exceptionally strong rear inflow across its back edge (Fig. 10b). The mesoscale model captures the evolution of this rear inflow, although its magnitude is underestimated because of the limited horizontal resolution and possibly the use of the full precipitation terminal velocity. Our discussion focuses on the development of this back-edge rear inflow and not on the internal component of the RTF flow, which is not resolved by the mesoscale model.

As discussed by ZG, the large-scale environment of the squall line provided an approximately 200-mb-deep layer of ambient RTF flow behind the squall line of magnitude $4\text{--}8 \text{ m s}^{-1}$ (Fig. 17a). The strong ambient RTF flow resulted from the orientation of the squall line with respect to the large-scale flow at midlevels (Fig. 12b). The simulated RTF flow crossed the back edge of the stratiform precipitation region between 660 and 320 mb (Figs. 17b,c), comparable to the levels observed by radar (Fig. 10b, 680–360 mb) and in the rawinsonde composite of Gallus and Johnson (1991). At 0100 UTC (not shown), the leading edge of the RTF current was slightly enhanced and dipped downward at the back

edge of the precipitation aloft. The downward protrusion of the RTF flow began with the onset of sublimative cooling and mesoscale descent (not shown). By 0200 UTC (14 h) (Fig. 17a), the magnitude of the RTF flow at the rear edge of the squall line had increased by 4 m s^{-1} . The rear inflow reached maximum strength ($>12 \text{ m s}^{-1}$) by 0400 UTC (Fig. 17b), weakened by 0600 UTC (Fig. 17c), and then reintensified by 0800 UTC (Fig. 17d). During this period, the rear inflow penetrated further into the storm and to lower levels. The strong and relatively steady mesoscale descent between 0200 and 0800 UTC (Fig. 18) suggests that sublimative cooling and downward momentum transport contributed to this evolution of the rear inflow (Rutledge et al. 1988; ZG; Gao et al. 1990; Stensrud et al. 1991).

The development of the rear inflow is further elucidated by examining the evolution of the θ' and z' fields (Figs. 19 and 20). Figures 17 and 18 indicate the locations of features in these thermodynamic fields relative to the squall line's precipitation and vertical motion fields. At 0200 UTC (14 h), a large positive anomaly of θ' occurred in the upper troposphere in association with the intense resolvable-scale updraft (Figs. 18a and 19a, $x \approx 400 \text{ km}$). It was produced by condensation heating during the early stages of the storm and then maintained at later times by continued condensation within the ascending FTR flow. Cooler air associated

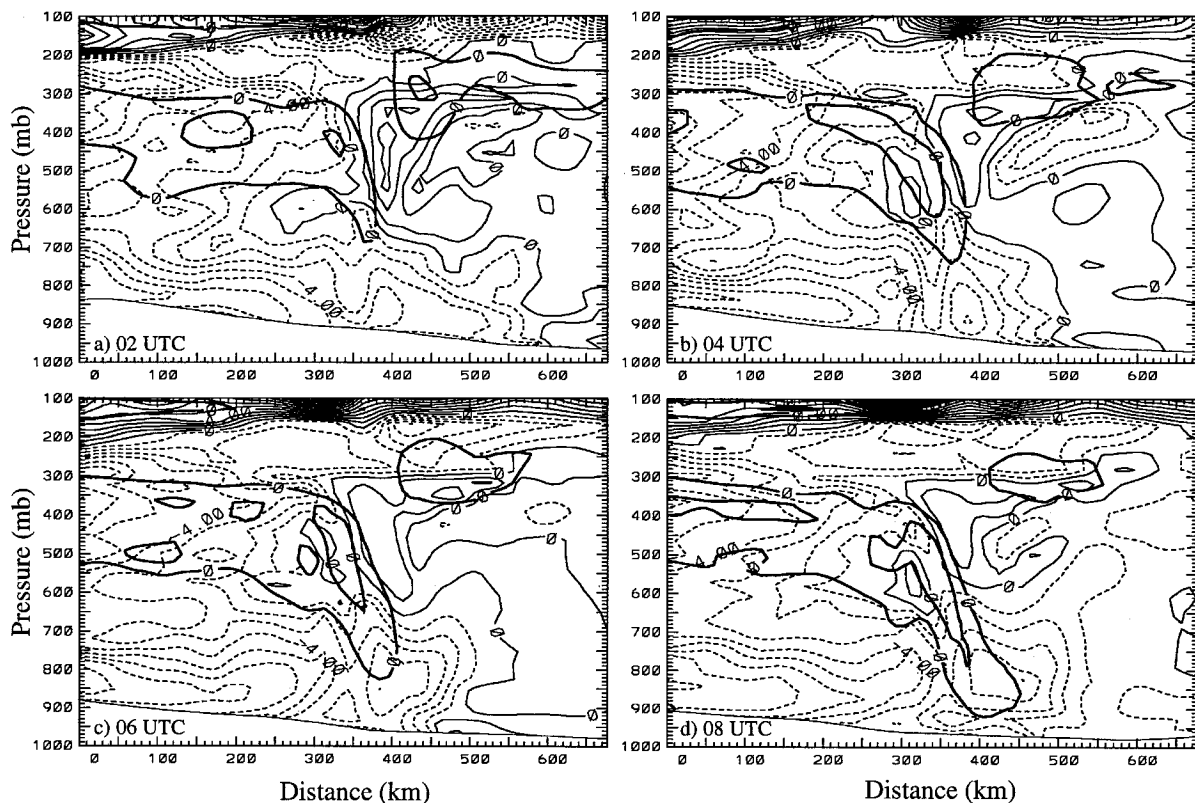


FIG. 19. Vertical cross sections of deviations of potential temperature from a mean profile at the leading edge of the cross sections on 11 June 1985. The contour interval is 1 K and solid (dashed) lines indicate positive (negative) values. Heavy solid lines are contours of RTF velocities at 0 and 8 m s^{-1} .

with the convectively generated cold pool and with the larger-scale baroclinic system was at low levels. In hydrostatic balance with the θ' field, z' shows a convectively generated mesohigh in the upper troposphere ($x \approx 400$ km, $p \approx 330$ mb) and mesolow ($x \approx 400$ km, $p \approx 680$ mb) and presquall low ($x \approx 460$ km, $p \approx 750$ mb) in the lower troposphere (dashed line labeled T1 in Fig. 20a). The mesolow and presquall low were local enhancements of the large-scale trough, within which the squall line formed (Figs. 8a and 12a) and were formed by the squall line's modifications of the thermal field.

The zone of strong potential temperature gradient at upper levels (i.e., at 400 mb in Figs. 14a–c) is evident to the rear of the positive θ' anomaly in Fig. 19. Prior to 0200 UTC, this potential temperature gradient zone was nearly vertically oriented and produced no significant features in the height field above 500 mb. However, by 0200 UTC (Figs. 19a and 20a), this zone developed a significant tilt toward the cold air and the resulting vertical gradient in buoyancy contributed to a weak trough between 550 and 350 mb at $x \approx 300$ –360 km (the upper portion of T1 in Fig. 20a). This trough was responsible for the initial acceleration of the mid-to upper-tropospheric RTF flow. By 0400 UTC (16 h) (Figs. 19b and 20b), adiabatic temperature increases as-

sociated with strong unsaturated mesoscale descent intensified the wake trough at the back edge of the precipitation ($x \approx 300$ –350 km, T2 in Fig. 20b). The wake trough extended vertically from the surface to almost 500 mb and had maximum intensity near 650 mb. Near 600 mb and 350 km, the temperature gradient associated with the negative buoyancy anomaly in Fig. 14b,d was located between the warm θ' anomaly generated by the mesoscale descent and a vertical extension of the low-level cold pool associated with sublimative cooling. The midlevel warming associated with the mesoscale descent and a reduction of the positive potential temperature perturbations in the weakening resolvable-scale updraft produced a reduction of the upper-level potential temperature gradient along the back edge of the system. Consequently, the trough at the back edge of the squall line in the 500–300-mb layer (upper portion of T1) and the RTF acceleration of the rear inflow weakened somewhat after 0400 UTC. Between 0600 and 0800 UTC (Figs. 17c,d and 20c,d), as the wake trough weakened, the rear inflow strengthened again and advanced forward and downward into the leading portion of the squall line.

In a high-resolution, two-dimensional model simulation of the 10–11 June squall line, Yang and Houze (1995) found that a secondary maximum in RTF flow

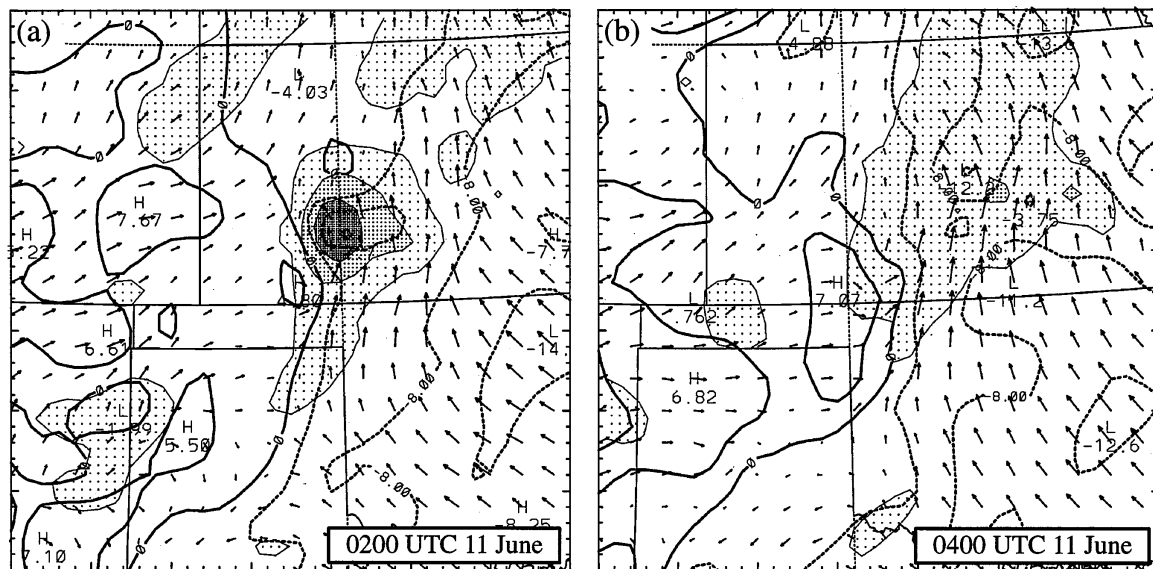


FIG. 21. Same as in Figs. 13a and 13b but for the case with sublimative cooling removed.

resolution model simulation and the observations and mesoscale model results suggests that the higher altitude and greater strength of the rear inflow in the latter information were a consequence of the environmental influences on the squall line. Specifically, as suggested by ZG, the large-scale baroclinic environment provided a deep layer in the upper troposphere of persistent and favorable RTF flow that accounted for approximately half of the intensity of the rear inflow. The high-resolution model results thus *isolate* the character of the circulations forced by the internal physics and dynamics of the squall line, while the mesoscale model results show the *added* effect of the larger-scale environment. The location of the maximum rear inflow above the 0°C level and the rapid acceleration of the rear inflow near the back edge of the squall line following the onset of strong cooling there, as shown in Figs. 13, 16, and 17, suggest that sublimative cooling played a significant role in the added effect of the large-scale environment on the rear inflow. The higher-resolution model simulations (Gallus and Johnson 1995; Yang and Houze 1995) show that sublimation does not play a significant role in the ability of the squall line to generate RTF flow by virtue of its own internal physics and dynamics.

3) EFFECTS OF GRID-RESOLVABLE SUBLIMATIVE AND EVAPORATIVE COOLING ON THE DEVELOPMENT OF THE REAR INFLOW

Sensitivity tests performed with the MM5 give insight into the way in which sublimative and evaporative cooling enhanced the large-scale environment's contribution to the strength of the rear inflow. Zhang and Gao (1989) found that when ice microphysics were excluded in their mesoscale-model simulation of the 10–11 June squall

line, the mesoscale circulations, including the rear inflow, were much weaker. They also found that when grid-resolvable evaporative and sublimative cooling were turned off in their simulation, the mesoscale descent and rear inflow, and the squall line as a whole, were much weaker. It is uncertain from their results whether the reduced strength of these features was caused more by the neglect of evaporation or sublimation. To determine which process produced the greater impact, we remove the *resolvable-scale* evaporative and sublimative cooling separately. These simulations, referred to as the NOEVP and NOSUB simulations, respectively, were started from the 0000 UTC (12 h) 11 June model fields (shortly before the initial development of the rear inflow) so that the cooling effects on the subsequent development could be examined.

Figure 21 shows the snow mixing ratios and storm-relative flow at 500 mb for the NOSUB simulation. This simulation showed only slight differences from the control run at 500 mb at 0200 UTC (14 h) (compare Fig. 21a with 13a). However, by 0400 UTC (Fig. 21b), the squall line was significantly weaker and the core of strong rear inflow did not develop. Strong mesoscale descent also failed to form and the resolvable-scale updraft (and the positive θ' anomaly) rapidly weakened. The weakening of the positive θ' anomaly and the lack of sublimative cooling prevented the formation of the strong horizontal buoyancy gradients along the back edge of the storm; hence, the midlevel trough and the strong rear inflow did not form. These results show that accurate simulation with the mesoscale model of the rear inflow, and the 10–11 June squall line in general, depends significantly on the inclusion of sublimative cooling.

In the NOEVP simulation (not shown), the evolution

of the squall line and the rear inflow differed little from the control simulation over the first 4–6 h except that the vertical motions in the squall line were somewhat weaker. The lack of sensitivity to *resolvable-scale* evaporation was caused in part by the coarse horizontal resolution of the mesoscale model simulation and the retention of parameterized downdrafts in the NOEVP simulation. Yang and Houze (1995), using a high-resolution model, found dramatic differences in the structure of the squall line and its associated circulations when the cooling from evaporation was removed. Without evaporation, the squall line simulated by the high-resolution model lacked a surface cold pool and the convective updrafts were nearly upright or tilted slightly downshear compared to the upshear tilt obtained when evaporation was included in the model. Gallus and Johnson (1995) showed that the strength of the mesoscale circulations within the stratiform region were strongly dependent on evaporative cooling. In the mesoscale model (with *resolvable-scale* evaporation included), the cooling by evaporation associated with mesoscale descent was confined to a nearly 50-km-wide region near the back edge of the squall line (Figs. 17 and 18). A significant portion of the total evaporative cooling at low levels was associated with the parameterized downdrafts and was not excluded in the NOEVP simulations. In their mesoscale model simulation of the 10–11 June squall line, ZG found that the removal of parameterized downdrafts, but retention of *resolvable-scale* cooling, caused the squall line to propagate more slowly and led to a weaker cold pool, mesohigh, and wake low. These studies indicate that removal of both *resolvable-scale* and parameterized evaporation would likely yield more significant differences than the removal of *resolvable-scale* evaporation alone.

The results of the mesoscale model calculations of this study taken together with the results of the high-resolution model calculations of Yang and Houze (1995) thus show that both sublimation and evaporation are important in the evolution of the squall-line system and its associated mesoscale circulations but that the scales on which the sublimation and evaporation operate in the mesoscale model are different. This study shows that on the *resolvable scale* of the mesoscale model sublimation of ice is important; specifically, it intensifies the ambient rear inflow where it interacts with the rear portion of the precipitation area at midlevels. Evaporation on the *resolvable scale* has much less effect. The Yang and Houze (1995) study shows that on smaller scales, internal to the cloud system, ice phase microphysics are also important; however, it is the evaporation of the rain formed by the melting of ice particles (in downdraft regions) that is important, and sublimation of ice particles plays no significant role. In the mesoscale model, evaporation internal to the cloud system takes place on the subgrid scales as part of the convective parameterization.

5. Effects of the large-scale environment on squall-line dissipation

Concomitant with the descent and forward penetration of the rear inflow (primarily after 0400 UTC) was a weakening and retreat of the low-level inflow (the core of strongest low-level inflow weakened and was located further upstream as time progressed), a substantial reduction of the low-level across-line wind shear (below 750 mb ahead of the squall line) and a rapid weakening of the ascent (Figs. 17 and 18). ZGP suggested that the squall line weakened as it moved into an environment with less convective instability. The evolution of the across-line flow (Fig. 17) supports Johnson and Hamilton's (1988) assertion that reduction of the low-level wind shear may also have contributed to the decline of the storm by reducing the effectiveness of the cold pool in sustaining nearly upright convection along the gust front. According to Rotunno et al. (1988), Xu (1992), and Xu and Moncrieff (1994), the weakening of the low-level shear would lead to weaker and shallower updrafts that tilt strongly rearward with height. As suggested by ZGP, these updrafts are eventually cut off from the boundary layer by the descending rear inflow. It will be shown below that the changes in the strength of the low-level inflow and vertical shear are related to changes in the larger-scale pressure field associated with cyclogenesis over Missouri ahead of the squall line [see Zhang and Harvey (1995) for a discussion of the evolution of the cyclone].

Figure 20 provides a partial explanation for the retreat of the low-level inflow seen in Fig. 17. After 0200 UTC (14 h) (Fig. 20b–d), the presquall low advanced ahead of the line and rapidly weakened. Since the leading edge of the strongest low-level inflow was coincident with the mesolow (Figs. 17 and 20), it too advanced increasingly farther ahead of the squall line.

The forward advance and weakening of the low-level trough and the reduction of the low-level wind shear was apparently associated with the evolution of the meso- α -scale pressure field associated with the initial stages of cyclogenesis over Missouri. Figure 22 shows the evolution of the sea level pressure and 1-h rainfall fields between 0300 and 0900 UTC (15 and 21 h). At 0300 UTC (Fig. 22a), the surface trough was located ahead of the southern and central portions of the squall line over Oklahoma and Texas. At the northern end of the trough near the Oklahoma–Kansas border, the winds abruptly changed from southerly to southeasterly. This southeasterly flow produced the strong low-level inflow seen in Figs. 17a and 17b. A weak low was associated with the remnants of the 10 June MCS over western Missouri. By 0600 UTC (18 h) (Fig. 22b), the presquall trough elongated and connected with the low over Missouri, where a more organized cyclonic circulation was developing. The flow ahead of the squall line was southerly such that the component of the flow directed toward the squall line was weaker (see also Fig. 17c). After

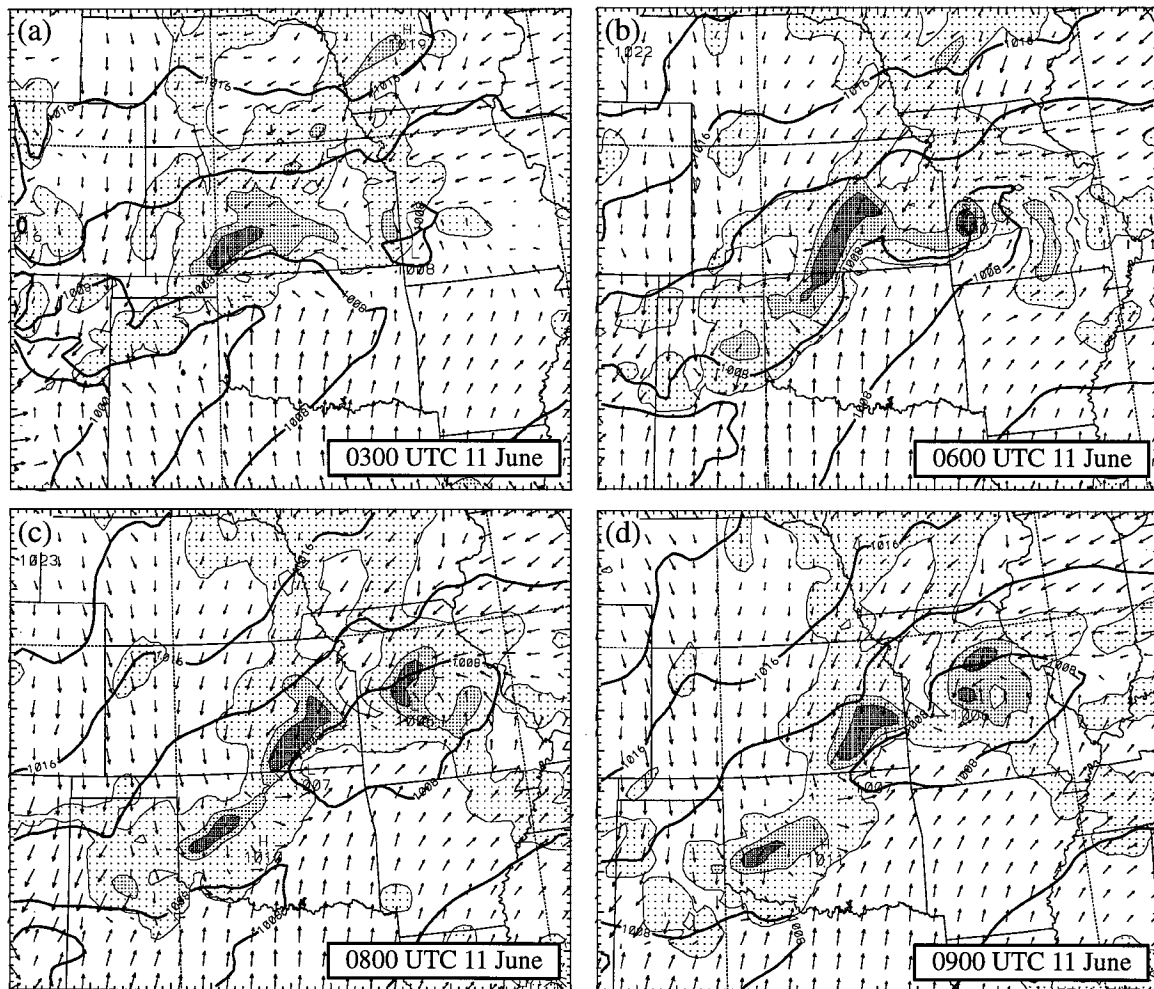


FIG. 22. Sea level pressure, total 1-h rainfall (parameterized and explicit), and surface vector winds. Sea level pressure is contoured at 4-mb intervals. Shading levels correspond to rainfall depths of 0.1, 5, and 10 mm. Axis tick marks are drawn every 20 km. Velocity vectors 60 km in length correspond to 15 m s^{-1} .

0600 UTC (Figs. 22c,d), the presquall trough split over Oklahoma and formed a closed low near the convection over Missouri and ahead of the northern portion of the 10–11 June squall line. The split in the presquall trough coincided with the initial split in the rainfall over northern Oklahoma and was partially caused by an increase in sea level pressures associated with a forward surge of the outflow from the 10–11 June squall line. This enhanced outflow occurred in association with the forward and downward penetration of the rear inflow. The deepening of the low and intensification of the cyclonic circulation over Missouri between 0300 and 0900 UTC apparently reduced the component of the presquall flow normal to the line below 800 mb (Fig. 17) as the flow changed from southeasterly to southwesterly ahead of the central portion of the squall line over Oklahoma. Meanwhile, the presquall flow above 800 mb remained relatively steady (Fig. 17). Thus, the reduction of the low-level inflow caused by the larger-scale cyclogenesis

led to a reduction of the low-level wind shear in the presquall environment. The weaker wind shear likely interacted with the cold pool in such a way that lifting at the gust front was insufficient to maintain deep convection (Rotunno et al. 1988; Xu 1992; Xu and Moncrieff 1994).

6. Conclusions

Mesoscale analysis of surface observations and mesoscale modeling results show that the 10–11 June squall line, contrary to prior studies, did not form entirely ahead of a cold front. The primary environmental features leading to the initiation and organization of the 10–11 June 1985 squall line were a low-level trough in the lee of the Rocky Mountains and a midlevel short-wave trough. Three additional mechanisms were active: a southeastward-moving cold front formed the northern part of the line, convection along the western edge of

cold air produced by prior convection over Oklahoma and Kansas formed the central part of the line, and convection forced possibly by cold convective outflow near the lee trough axis formed the southern portion of the line.

A simulation of the squall line using the PSU–NCAR mesoscale model (MM5) successfully reproduced the squall line's initiation and the general evolution of the precipitation field, including the split of the storm in its decaying stage and the development of convective storms ahead of the squall line in Missouri.

The mesoscale model shows that the horizontal as well as the vertical variability of the large-scale environment significantly influenced the mesoscale circulations associated with the squall line. In particular, the distribution of the along-line velocities was at least partly attributable to the larger-scale circulations associated with the lee trough and midlevel baroclinic wave. The formation of the squall line near or along the trough axis at low to midlevels led to a deep layer of negative (northeasterly) along-line velocities to the rear of the convective line.

The large-scale environment also favored the development of significant across-line circulations, including stronger than average rear inflow at the rear of the stratiform precipitation region (Smull and Houze 1987), by providing significant ambient RTF flow in a 200-mb layer to the rear of the squall line (ZGP; ZG). The ambient RTF flow resulted from the squall line's nearly perpendicular orientation to strong west-northwesterly flow at upper levels. Line-end effects (Skamarock et al. 1994) and the generation of horizontal buoyancy gradients at the back edge of the system (Weisman 1992) combined with this ambient RTF flow to concentrate the strongest convection and back-edge sublimative cooling along the central portion of the line, which then produced a core of maximum rear inflow with a horizontal scale of approximately 100–200 km. The maximum in rear inflow was located primarily in the 600–350-mb layer. It occurred immediately to the rear of the maximum snow mixing ratios and moved with the speed and direction of the band of heaviest precipitation. The formation of the rear-inflow core followed the onset of strong sublimative cooling at the back edge of the storm.

The acceleration of the ambient RTF flow to form the core of maximum rear inflow was associated with a mid-to upper-level mesoscale trough that formed immediately to the rear of the maximum snow mixing ratios. The mesoscale trough developed in response to a vertically sloping zone of strong buoyancy gradient, associated with condensation heating in the upward-sloping FTR flow and sublimative cooling in the mesoscale downdraft, near the back edge of the squall line. This trough, and the rear-inflow maximum, did not form when resolvable-scale sublimative cooling was turned off in the model. In contrast, removal of resolvable-scale evaporative cooling produced only minor changes in rear-inflow strength; however, evaporation in para-

meterized downdrafts remained important for accurate simulation of the rear inflow. The intensification of the RTF flow by the trough and its transport by mesoscale descent led to the forward and downward penetration of the rear inflow into the squall line. This penetration of the RTF flow into the heart of the storm ultimately contributed to the split and decay of the stratiform rainfall.

Both mesoscale (ZG) and high-resolution (Yang and Houze 1995) models indicate that ice-phase microphysics are crucial; neither model produces a completely realistic simulation of the 10–11 June squall line without them. Nor does either model alone clearly convey all of the physics and dynamics of the storm when ice-phase microphysics are included. The mesoscale model conveys the broader features but does not accurately represent smaller-scale microphysical processes. The high-resolution model conveys the small-scale organization of microphysics but cannot represent the features arising from the interaction of the squall-line system with the horizontally varying large-scale environmental flow.

Because of the low fall speeds of ice, the wind (in both models) distributes the ice particles horizontally. As the ice particles fall below the cloud base, they sublimate in the post-stratiform precipitation region (rear anvil), and they melt and evaporate in the convective and stratiform precipitation regions. The two models, viewed together, show that there are [as suggested by Smull and Houze (1987) and ZG] both a RTF flow intensification internal to the convective system and an augmentation of the RTF flow by the environmental cross-line wind component. The mesoscale model shows additionally that this augmentation is not just a linear addition of a large-scale flow component to the cloud-system circulation, but rather the ambient flow is intensified by a microphysical–dynamical interaction involving the sublimation of ice and an associated sharpening of the large-scale pressure trough at the back edge of the cloud system.

The two types of model results both show that evaporation of raindrops formed by the melting ice is crucial to simulating the RTF flow accurately, but that the evaporation occurs on smaller scales and is largely a parameterized effect when the grid scale is about 20 km or greater. The sublimation, on the other hand, which is also crucial to reproducing the observed rear inflow, is a larger-scale effect, which is represented well in the mesoscale model because of the large horizontal extent of the stratiform ice cloud and snow region in the squall line and the inclusion of the horizontal structure and temporal variability of the large-scale environment.

The penetration of the rear inflow deeper into the storm at a time when the presquall thermodynamic environment was becoming less favorable for convection contributed to the dissipation of the central portion of the squall line (ZGP; ZG). The mesoscale model results suggest, however, that additional factors may have con-

tributed to the decay of the system. The evolution of the meso- α -scale pressure field near the surface apparently led to a reduction of the low-level inflow into the central portion of the line and to a reduction of the low-level vertical wind shear ahead of the squall line. The reduction of the low-level wind shear apparently decreased the effectiveness of the cold pool in sustaining deep, nearly upright convection along the gust front, thereby contributing to the decline of the squall line. The decreases in the low-level inflow and vertical wind shear were associated with veering of the presquall flow from southeasterly to southwesterly as cyclogenesis began over Missouri.

In this study, the focus was on the influence of the large-scale environment on the initiation, evolution, and dissipation of the squall line. Work is in progress that examines the upscale feedbacks of the 10–11 June squall line and the role of the convection in the cyclogenesis that occurred over Missouri in the later stages of the storm.

Acknowledgments. We thank Da-Lin Zhang and Ming-Jen Yang for providing their mesoscale (MM4) and high-resolution simulation output of the squall line to us. Brian Colle, James Steenburgh, Shuyi Chen, and Mark Stoelinga provided advice and guidance on the mesoscale model simulation and graphics production. Michael Biggerstaff provided the dual-Doppler radar data. Christopher Bretherton, Dale Durran, Richard Johnson, Morris Weisman, Da-Lin Zhang, and Conrad Ziegler provided helpful comments. G. C. Gudmundson edited the manuscript and Kay Dewar helped draft the figures. This research was sponsored by National Science Foundation Grant ATM-9409988.

REFERENCES

- Anthes, R. A., E.-Y. Hsie, and Y.-H. Kuo, 1987: Description of the Penn State/NCAR Mesoscale Model Version 4 (MM4). NCAR Tech. Note NCAR/TN-282, 66 pp. [Available from NCAR, P.O. Box 3000, Boulder, CO 80307.]
- Bartels, D. L., and R. A. Maddox, 1991: Midlevel cyclonic vortices generated by mesoscale convective systems. *Mon. Wea. Rev.*, **119**, 104–118.
- Benjamin, S. G., and N. L. Seaman, 1985: A simple scheme for improved objective analysis in curved flow. *Mon. Wea. Rev.*, **113**, 1184–1198.
- Biggerstaff, M. I., and R. A. Houze Jr., 1991a: Kinematic and precipitation structure of the 10–11 June 1985 squall line. *Mon. Wea. Rev.*, **119**, 3034–3065.
- , and —, 1991b: Midlevel vorticity structure of the 10–11 June 1985 squall line. *Mon. Wea. Rev.*, **119**, 3066–3079.
- , and —, 1993: Kinematics and microphysics of the transition zone of the 10–11 June 1985 squall line. *J. Atmos. Sci.*, **50**, 3091–3110.
- Bosart, L. F., and F. Sanders, 1981: The Johnstown flood of 1977: A long-lived convective storm. *J. Atmos. Sci.*, **38**, 1616–1642.
- Brandes, E. A., 1990: Evolution and structure of the 6–7 May 1985 mesoscale convective system and associated vortex. *Mon. Wea. Rev.*, **118**, 109–127.
- Braun, S. A., and R. A. Houze Jr., 1994: The transition zone and secondary maximum of radar reflectivity behind a midlatitude squall line: Results retrieved from Doppler radar data. *J. Atmos. Sci.*, **51**, 2733–2755.
- Chen, S., and W. R. Cotton, 1988: The sensitivity of a simulated extratropical mesoscale convective system to longwave radiation and ice-phase microphysics. *J. Atmos. Sci.*, **45**, 3897–3910.
- Chong, M., P. Amayenc, G. Scialom, and J. Testud, 1987: A tropical squall line observed during the COPT 81 experiment in West Africa. Part I: Kinematic structure inferred from dual-Doppler radar data. *Mon. Wea. Rev.*, **115**, 670–694.
- Cunning, J. B., 1986: The Oklahoma–Kansas Preliminary Regional Experiment for STORM-Central. *Bull. Amer. Meteor. Soc.*, **67**, 1478–1486.
- Davis, C. A., and M. L. Weisman, 1994: Balanced dynamics of simulated, long-lived, mesoscale convective systems. *J. Atmos. Sci.*, **51**, 2005–2030.
- Dudhia, J., 1993: A nonhydrostatic version of the Penn State–NCAR Mesoscale Model: Validation tests and simulation of an Atlantic cyclone and cold front. *Mon. Wea. Rev.*, **121**, 1493–1513.
- Fovell, R. G., and Y. Ogura, 1988: Numerical simulation of a midlatitude squall line in two dimensions. *J. Atmos. Sci.*, **45**, 3846–3879.
- Fritsch, J. M., and C. F. Chappell, 1980: Numerical prediction of convectively driven mesoscale pressure systems. Part I: Convective parameterization. *J. Atmos. Sci.*, **37**, 1722–1733.
- , J. D. Murphy, and J. S. Kain, 1994: Warm core mesovortex amplification over land. *J. Atmos. Sci.*, **51**, 1780–1807.
- Gallus, W. A., Jr., and R. H. Johnson, 1991: Heat and moisture budgets of an intense midlatitude squall line. *J. Atmos. Sci.*, **48**, 122–146.
- , and —, 1995: The dynamics of circulations within the trailing stratiform regions of squall lines. Part II: Influence of the convective line and ambient environment. *J. Atmos. Sci.*, **52**, 2188–2211.
- Gao, K., D.-L. Zhang, M. W. Moncrieff, and H.-R. Cho, 1990: Mesoscale momentum budget in a midlatitude squall line: A numerical case study. *Mon. Wea. Rev.*, **118**, 1011–1028.
- Houze, R. A., Jr., 1993: *Cloud Dynamics*. Academic Press, 573 pp.
- , S. A. Rutledge, M. I. Biggerstaff, and B. F. Smull, 1989: Interpretation of Doppler weather radar displays in midlatitude mesoscale convective systems. *Bull. Amer. Meteor. Soc.*, **70**, 608–619.
- , B. F. Smull, and P. Dodge, 1990: Mesoscale organization of springtime rainstorms in Oklahoma. *Mon. Wea. Rev.*, **118**, 613–654.
- Johnson, R. H., and P. J. Hamilton, 1988: The relationship of surface pressure features to the precipitation and airflow structure of an intense midlatitude squall line. *Mon. Wea. Rev.*, **116**, 1444–1472.
- , and D. L. Bartels, 1992: Circulations associated with a mature-to-decaying midlatitude mesoscale convective system. Part II: Upper-level features. *Mon. Wea. Rev.*, **120**, 1301–1320.
- Klimowski, B. A., 1994: Initiation and development of rear inflow within the 28–29 June 1989 North Dakota mesoconvective system. *Mon. Wea. Rev.*, **122**, 765–779.
- Lafore, J.-P., and M. W. Moncrieff, 1989: A numerical investigation of the organization and interaction of the convective and stratiform regions of tropical squall lines. *J. Atmos. Sci.*, **46**, 521–544.
- LeMone, M. A., 1983: Momentum transport by a line of cumulonimbus. *J. Atmos. Sci.*, **40**, 1815–1834.
- , G. M. Barnes, and E. J. Zipser, 1984: Momentum flux by lines of cumulonimbus over the tropical oceans. *J. Atmos. Sci.*, **41**, 1914–1932.
- Loehrer, S. M., and R. H. Johnson, 1995: Surface pressure and precipitation life cycle characteristics of PRE-STORM mesoscale convective systems. *Mon. Wea. Rev.*, **123**, 600–621.
- Manning, K. W., and P. L. Haagenson, 1992: Data ingest and objective analysis for the PSU/NCAR modeling system: Programs DATAGRID and RAWINS. NCAR Tech. Note NCAR/TN-376+IA, 209 pp. [Available from NCAR, P. O. Box 3000, Boulder, CO 80307.]

- Orlanski, I., 1975: A rational subdivision of scales for atmospheric processes. *Bull. Amer. Meteor. Soc.*, **56**, 527–530.
- Raymond, D. J., and H. Jiang, 1990: A theory for long-lived mesoscale convective systems. *J. Atmos. Sci.*, **47**, 3067–3077.
- Rotunno, R., J. B. Klemp, and M. L. Weisman, 1988: A theory for strong, long-lived squall lines. *J. Atmos. Sci.*, **45**, 463–485.
- Roux, F., 1985: Retrieval of thermodynamic fields from multiple Doppler-radar data using the equations of motion and the thermodynamic equation. *Mon. Wea. Rev.*, **113**, 2142–2157.
- Rutledge, S. A., R. A. Houze Jr., M. I. Biggerstaff, and T. Matejka, 1988: The Oklahoma–Kansas mesoscale convective system of 10–11 June 1985: Precipitation structure and single-Doppler radar analysis. *Mon. Wea. Rev.*, **116**, 1409–1430.
- Skamarock, W. C., M. L. Weisman, and J. B. Klemp, 1994: Three-dimensional evolution of simulated long-lived squall lines. *J. Atmos. Sci.*, **51**, 2563–2584.
- Smull, B. F., and R. A. Houze Jr., 1985: A midlatitude squall line with a trailing region of stratiform rain: Radar and satellite observations. *Mon. Wea. Rev.*, **113**, 117–133.
- , and —, 1987: Rear inflow in squall lines with trailing stratiform precipitation. *Mon. Wea. Rev.*, **115**, 2869–2889.
- , and J. A. Augustine, 1993: Multiscale analysis of a mature mesoscale convective complex. *Mon. Wea. Rev.*, **121**, 103–132.
- Stensrud, D. J., R. A. Maddox, and C. L. Ziegler, 1991: A sublimation-initiated mesoscale downdraft and its relation to the wind field below a precipitating anvil cloud. *Mon. Wea. Rev.*, **119**, 2124–2139.
- Szeto, K. K., and H.-R. Cho, 1994: A numerical investigation of squall lines. Part III: Sensitivity to precipitation processes and the Coriolis force. *J. Atmos. Sci.*, **51**, 1341–1351.
- Washington, W. M., and D. P. Baumhefner, 1975: A method of removing Lamb waves from initial data for primitive equation models. *J. Appl. Meteor.*, **14**, 114–119.
- Weisman, M. L., 1992: The role of convectively generated rear-inflow jets in the evolution of long-lived mesoconvective systems. *J. Atmos. Sci.*, **49**, 1826–1847.
- , 1993: The genesis of severe, long-lived bow echoes. *J. Atmos. Sci.*, **50**, 645–670.
- , W. C. Skamarock, and J. B. Klemp, 1997: The resolution dependence of explicitly modeled convective systems. *Mon. Wea. Rev.*, **125**, 527–548.
- Xu, Q., 1992: Density currents in shear flows—A two fluid model. *J. Atmos. Sci.*, **49**, 511–524.
- , and M. W. Moncrieff, 1994: Density current circulations in shear flows. *J. Atmos. Sci.*, **51**, 434–446.
- Yang, M.-J., and R. A. Houze Jr., 1995: Sensitivity of squall-line rear inflow to ice microphysics and environmental humidity. *Mon. Wea. Rev.*, **123**, 3175–3193.
- Zhang, D.-L., 1989: The effect of parameterized ice microphysics on the simulation of vortex circulation with a mesoscale hydrostatic model. *Tellus*, **41A**, 132–147.
- , 1992: Formation of a cooling-induced mesovortex in the trailing stratiform region of a midlatitude squall line. *Mon. Wea. Rev.*, **120**, 2763–2785.
- , and R. A. Anthes, 1982: A high-resolution model of the planetary boundary layer—Sensitivity tests and comparisons with SESAME-79 data. *J. Appl. Meteor.*, **21**, 1594–1609.
- , and J. M. Fritsch, 1986: Numerical simulation of the meso- β scale structure and evolution of the 1977 Johnstown flood. Part I: Model description and verification. *J. Atmos. Sci.*, **43**, 1913–1943.
- , and —, 1987: Numerical simulation of the meso- β scale structure and evolution of the 1977 Johnstown flood. Part II: Inertially stable warm-core vortex and the mesoscale convective complex. *J. Atmos. Sci.*, **44**, 2593–2612.
- , and —, 1988: A numerical investigation of a convectively generated, inertially stable, extratropical warm-core mesovortex over land. Part I: Structure and evolution. *Mon. Wea. Rev.*, **116**, 2660–2687.
- , and K. Gao, 1989: Numerical simulation of an intense squall line during 10–11 June 1985 PRE-STORM. Part II: Rear inflow, surface pressure perturbations, and stratiform precipitation. *Mon. Wea. Rev.*, **117**, 2067–2094.
- , and R. Harvey, 1995: Enhancement of extratropical cyclogenesis by a mesoscale convective system. *J. Atmos. Sci.*, **52**, 1107–1127.
- , H.-R. Chang, N. L. Seaman, T. T. Warner, and J. M. Fritsch, 1986: A two-way interactive nesting procedure with variable terrain resolution. *Mon. Wea. Rev.*, **114**, 1330–1339.
- , K. Gao, and D. B. Parsons, 1989: Numerical simulation of an intense squall line during 10–11 June 1985 PRE-STORM. Part I: Model verification. *Mon. Wea. Rev.*, **117**, 960–994.